Nano Research

Open Access

Research Article

3D bioprinted advanced cartilage organoids with engineered magnetic nanoparticles polarized-BMSCs/alginate/gelatin for cartilage tissue regeneration

Zhiyu Ding[1,2], Junjie Huang[1,2], Yijun Ren[3], Ning Tang[1], Xin Luo[1], Huancheng Zhu[2], Xu Cao[1,2] ✉, Ming Zhao[2] ✉, and Song Wu[1] ✉

[1] *Department of Orthopedics, Third Xiangya Hospital of Central South University, Changsha 410013, China*
[2] *Lab of Research and Engineering of Cell Therapy Technology, Hangzhou Institute of Medicine Chinese Academy of Sciences, Hangzhou 310018, China*
[3] *Department of Neurology, Xiangya Hospital of Central South University, Changsha 410028, China*

Cite this article: *Nano Research*, **2025**, *18*, 94907084. https://doi.org/10.26599/NR.2025.94907084

ABSTRACT: Cartilage defects are commonly observed in orthopedic clinical studies. Owing to the unique structure of cartilage tissue, current clinical treatments cannot fully address this issue. Cartilage organoids are three-dimensional (3D) active tissue structures constructed *in vitro* to mimic the structure and function of natural cartilage tissue and can be utilized for disease research and cartilage repair. In this study, we engineered MNPs-BMSCs by introducing magnetic nanoparticles (MNPs) into bone marrow mesenchymal stem cells (BMSCs). Under the influence of the magnetic field induced by the MNPs, MNPs-BMSCs became polarized, significantly enhancing their aggregation, migration, and chondrogenic differentiation capabilities. We then used these engineered MNPs-BMSCs as seed cells and applied 3D bioprinting technology to construct an advanced cartilage organoid using a MNPs-BMSC/alginate/gelatin matrix. This structure partially mimics the middle layer of a cartilage. The advanced cartilage organoid demonstrated superior chondrogenic differentiation ability and mechanical properties *in vitro*. It significantly enhanced tissue repair in cartilage defect areas *in vivo*, restoring the normal structure of the cartilage layer. Overall, the engineered MNPs-BMSCs/alginate/gelatin advanced cartilage organoids offer a promising approach for studying cartilage tissue *in vitro* and advancing cartilage repair within the field of tissue engineering.

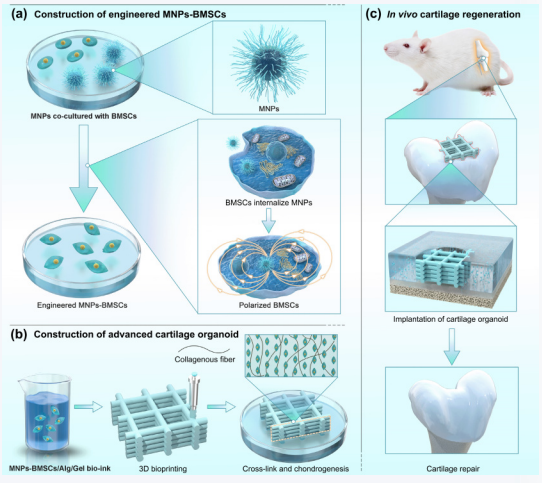

KEYWORDS: magnetic nanoparticles, cell polarization, three-dimensional (3D) bioprinting, cartilage organoid, cartilage repair

1 Introduction

Cartilage injury is a prevalent orthopedic condition that typically results in cartilage resorption, bone deterioration, and, ultimately, the onset of osteoarthritis [1]. The unique structure of cartilage, characterized by sparse vascular distribution, low cell density, and limited cell migration ability, results in a limited capacity for self-repair, thereby exacerbating the progression of osteoarthritis [2]. Several new technologies have been applied in clinical practice for cartilage tissue engineering to repair osteoarthritis-related cartilage defects; however, all have significant limitations [3]. Mesenchymal stem cells (MSCs), particularly bone marrow-derived mesenchymal stem cells (BMSCs), are widely used in cartilage tissue engineering [4, 5]. However, enhancing the chondrogenic differentiation of BMSCs and improving their efficiency in cartilage repair remain pressing issues [6, 7].

Cell polarization refers to the organized establishment of asymmetry within a cell. Cellular functions are compartmentalized within organelles; hence, many cellular functions become more

Received: August 6, 2024; **Revised:** September 29, 2024
Accepted: October 17, 2024

✉Address correspondence to Song Wu, xy3ws1969@hotmail.com; Ming Zhao, zmingys@sina.com; Xu Cao, hughcaoxu@hotmail.com

efficient when divided along the polarization axis [8]. Cell polarity is crucial in self-renewal and stem cell differentiation [9]. Simultaneously, feedback interactions between cell polarity, mechanics, and cell fate are vital mechanisms in tissue self-organization [10]. However, the current research and applications of stem cell polarity changes in cartilage tissue engineering remain unexplored [3].

Magnetic nanoparticles (MNPs) are an essential class of nanoparticles typically composed of pure metals, such as iron (Fe), cobalt (Co), nickel (Ni), rare earth metals, or mixtures of metals and polymers [11]. They are used in various medical applications, including hyperthermia treatment for cancer, controlled drug release, magnetic resonance imaging, and biosensing [12, 13]. Owing to their excellent biocompatibility, MNPs have been widely used in bone tissue engineering, skin tissue engineering, tendon regeneration, and neural tissue engineering [14]. In recent years, MNPs have been increasingly applied in cartilage tissue engineering research, demonstrating their significant potential for cartilage tissue repair [6, 15–18]. Studies have shown that MNPs and magnetic fields can alter cell polarity in neuronal and breast cancer cell lines [19, 20]. However, further research is needed to utilize MNPs to alter the polarity of BMSCs and apply this knowledge in cartilage repair tissue engineering.

Organoids are self-renewing and self-organizing three-dimensional (3D) microstructures derived from the directed differentiation of stem or progenitor cells. They exhibit critical characteristics, structures, and functions that resemble certain aspects of organs [21, 22]. The structure of cartilage organoids should mimic the structure of normal cartilage tissue, including an extracellular matrix (ECM) rich in type II collagen and proteoglycans with embedded chondrocytes, closely resembling the layered architecture of cartilage [23, 24]. This primarily includes the middle and deep layers of cartilage, where cells and collagen fibers are arranged vertically [25]. Therefore, 3D bioprinting technology is essential for constructing appropriate structures for cartilage organoids. 3D bioprinting can be utilized to fabricate and integrate various cells, biocompatible materials, and supporting components into complex, functional living tissues. This method enables individual or multiple cells to be arranged in a specified form within biomaterials, facilitating the construction of functional 3D tissues using cells [26]. Alginate and gelatin, the most commonly used bio-inks for 3D bioprinting, exhibit excellent biocompatibility. The mechanical properties of these mixed hydrogels change appropriately under different temperatures, rendering them highly suitable for constructing cartilage organoids using 3D bioprinting [27, 28]. In recent years, most studies on cartilage organoids have focused primarily on innovative scaffold materials, with less emphasis on studying seed cells and simulating cartilage structures within organoids. Therefore, it is necessary to explore the construction of new types of cartilage organoids using modified engineered BMSCs and 3D bioprinting.

To address the challenges in applying BMSCs in cartilage repair, we developed an advanced cartilage organoid for *in vitro* cartilage research and defect repair (Scheme 1). This study utilized the

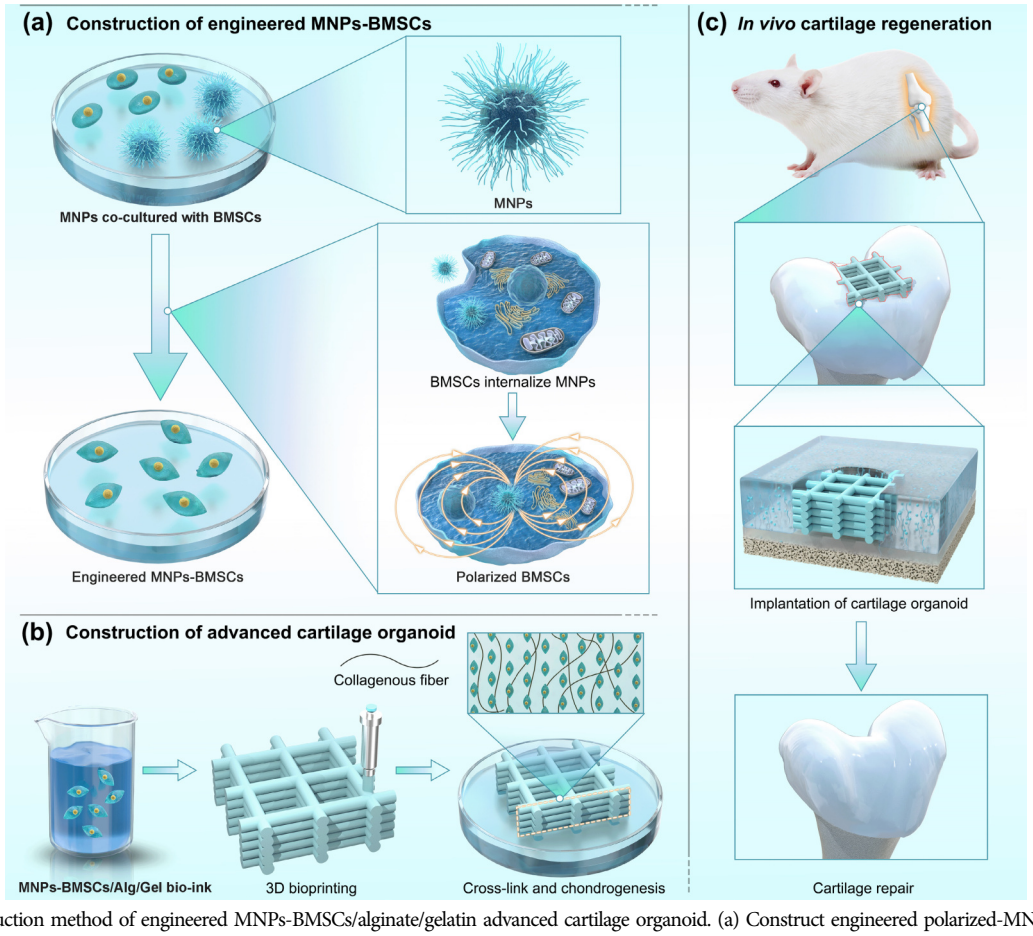

Scheme 1 Construction method of engineered MNPs-BMSCs/alginate/gelatin advanced cartilage organoid. (a) Construct engineered polarized-MNPs-BMSCs. (b) 3D bioprinting for constructing advanced cartilage organoids. (c) *In vivo* cartilage regeneration.

intrinsic magnetic field effects of MNPs to engineer BMSCs into polarized-engineered MNPs-BMSCs. These engineered stem cells exhibit significantly enhanced migratory and aggregation capabilities and superior chondrogenic differentiation potential. Utilizing these modified stem cells in conjunction with 3D bioprinting technology, we employed alginate/gelatin as a scaffold material to construct a cartilage organoid precursor. Following chondrogenic differentiation induced by TGF-β1, the precursor was transformed into an advanced cartilage organoid. This organoid better mimicked the fibrous and cellular arrangements of the middle zone of cartilage and demonstrated improved cell utilization and mechanical properties *in vitro*. *In vivo* studies revealed that this advanced cartilage organoid significantly enhanced cartilage regeneration. In summary, we proposed an innovative strategy for cartilage tissue engineering and *in vitro* cartilage research by constructing an advanced cartilage organoid using engineered magnetic nanoparticle-polarized BMSCs, alginate/gelatin, and 3D bioprinting.

2 Experimental

2.1 Materials

Unless otherwise stated, all reagents were procured from Thermo Fisher Scientific (USA). Magnetic nanoparticles, alginate, gelatin, and phalloidin-TRITC were purchased from Sigma-Aldrich (USA). All pathology staining reagent kits, live/dead staining kit, cell counting kit-8 (CCK-8), and EdU-click 488 kit were purchased from Biosharp technology (China). Specific primary antibodies against GM-130, Col-II, Aggrecan, Gapdh, and secondary antibodies (HRP and AF488) were purchased from Abcam (ab315486, ab313636, and ab52649, USA) and Aifang Biological (AF01904, AF06494, AFSA004, and AFSA005, China). The Sprague–Dawley (SD) rat bone marrow mesenchymal stem cell chondrogenic differentiation kit was obtained from Haixing Biosciences (China). All cell culture-related consumables and Matrigel were purchased from Corning (USA). All gene primers and IHC kits were purchased from Sango Biotech (China).

2.2 Morphology, characterization and cell biocompatibility of the nanoparticles

All MNPs are naked iron oxide nanoparticles (Fe_3O_4). The morphology, structure, and elemental composition of the MNPs were analyzed using transmission electron microscopy (TEM, JEOL JEM-2100plus) and scanning electron microscopy (SEM, JEOL JSM-IT800, Japan). The magnetic properties of the MNPs were evaluated using a vibrating-sample magnetometer (VSM, Quantum Design VersaLab, USA). The size distribution of the magnetic nanoparticles was determined using a nanoparticle size potentiometer (Malvern Zetasizer Nano ZS ZEN3600, UK).

The isolation and identification of rat BMSCs followed the methodology outlined in our previous publications [29]. The BMSCs were cultured in Dulbecco's Modified Eagle's Medium (DMEM) supplemented with 10% fetal bovine serum (FBS) and 1% penicillin–streptomycin. Nanoparticles of varying concentrations (0, 50, 100, and 150 μg/mL) were co-cultured with BMSCs for 4, 12, and 48 h. The CCK-8 assay and EdU click-488 were used to detect cell count and proliferative activity, respectively. Cell morphology and viability were assessed using live/dead staining, and Giemsa staining was employed to assess cellular genotoxicity.

2.3 The construction of engineered MNPs-BMSCs

After co-culturing BMSCs with 100 μg/mL nanoparticles, samples were collected at different time points (0, 0.5, 1, 2, 4, 8, 12, and 24 h) for Prussian blue staining and TEM detection to determine the optimal time point for nanoparticle internalization.

2.4 Cell polarity detection

The prepared MNP-BMSCs and control groups were fluorescently labeled with GM130 (Alexa Fluor 488) according to the standard protocol for immunofluorescence staining. Staining was performed using phalloidin, tetramethylrhodamine (TRITC), and DAPI. Fluorescence images were acquired using a confocal laser-scanning microscope (Nikon A1, Japan). The quantification analysis of cell polarity was done using Origin software (OriginLab, USA).

2.5 Transcriptomic analysis (mRNA-seq)

The collected MNP-BMSCs were designated as the MNPs group, and the BMSCs of the control group, which underwent no treatment, were designated as the BMSCs group. Total RNA from these cell samples was extracted using total RNA extraction reagent (TRIzol), followed by construction of the corresponding RNA libraries and subsequent high-throughput sequencing (performed by Applied Protein Technology, China). For sequencing data analysis, the DESeq software was used to identify differentially expressed genes (DEGs). In this study, genes with a p-value less than 0.05 and fold change greater than 2 or less than 0.5 were considered significantly differentially expressed. Additionally, for further bioinformatics analysis, gene ontology (GO) enrichment analysis, Kyoto Encyclopedia of Genes and Genomes (KEGG) pathway enrichment analysis, and Gene Set Enrichment Analysis (GSEA) were employed.

2.6 Cell invasion and migration and chondrogenic differentiation of MNPs-BMSC

Cell invasion experiments were conducted using 24-well Transwell plates. Matrigel was evenly spread onto the pre-cooled upper surface of the Transwell insert, with the entire process conducted on ice. Subsequently, the Transwell plate was placed in a 37 °C cell culture incubator to allow the Matrigel to solidify. Equal numbers of MNP-BMSCs and control group BMSCs were suspended in FBS-free DMEM and seeded onto the Matrigel, while the lower chambers were filled with DMEM containing 20% FBS. After 48 h, the Transwell chambers were stained with crystal violet; the upper layer of cells and Matrigel were wiped off, and photographs were taken under a microscope (Olympus CKX53, Japan).

For cell migration experiments, equal numbers of the two cell types were seeded in 12-well plates. After the cells were completely adhered to the plates, scratches of uniform width were made on the culture dish. Photographs were taken and analyzed at different time points (0, 24, and 48 h) to observe the progression of scratch closure.

For chondrogenic differentiation of the cells, total RNA was extracted after culturing the two cell types in the chondrogenic differentiation medium for 7 and 14 days. Subsequently, the gene expressions of Col-I, Col-II, Col-X, and Aggrecan were assessed using RT-qPCR (Bio-Rad CFX96 Touch, USA). Simultaneously, immunofluorescence staining was performed to assess the expression of Col-II and Aggrecan proteins in the cells, along with staining using Sirius red, Alcian blue, and Safranin-O.

In the chondrogenic pellet experiment, equal numbers of both

cell types were concentrated in a centrifuge (1300 rpm, 5 min). After carefully removing the culture medium, the chondrogenic differentiation medium was added. Cartilage pellets were collected after 14 days of culture, and frozen sections were prepared (Thermo Scientific NX70, USA). Immunohistochemical staining for Col-II and Aggrecan was performed, complemented with Sirius Red, Alcian blue, and Safranin-O staining.

2.7 Construction of 3D bioprinting scaffolds

To determine the optimal hydrogel ratio for organoid construction, a rotational rheometer (Thermo Scientific HAAKE MARS60, USA) was used to test the viscosity of the hydrogels (1% Gel + 9% Alg, 2% Gel + 8% Alg, 3% Gel + 7% Alg, 6% Gel + 4% Alg, and 5% Gel + 5% Alg). The tests included measuring the hydrogel viscosity at 18 °C across a shear rate range of 0.1–1000 s^{-1} and 4 °C under extremely low shear rate conditions (0.2 s^{-1}).

The Bio-Architect® WS, sourced from Regenovo (Hangzhou, China), was utilized as the 3D bioprinter. The sterilized 5% alginate and 5% gelatin were thoroughly mixed with chondrogenic differentiation medium at 37 °C on a shaker. BMSCs were added to each milliliter of the mixture at a concentration of 1×10^6 and thoroughly mixed to form a bioink suitable for 3D bioprinting. This bio-ink was transferred to sterile dedicated printing cartridges. After removing air bubbles by low-speed centrifugation, the cartridges were transferred to a preheated printer. The printing was executed using a pneumatic pressure-driven method. A rectangular model with cross-intersections, measuring 20 mm × 20 mm × 4 mm, was printed. The printing conditions included bio-ink temperature at 18 °C, printing platform temperature at 4 °C, pressure at 0.35 MPa, printing speed at 10 mm/s, extrusion advance at 300 ms, and retraction delay at 0.5 ms. Finally, the scaffold was cross-linked using 5% $CaCl_2$. The printing nozzle measured 0.21 mm, and the print consisted of 20 layers; various line spacings were utilized during the print process.

The porosity of the constructed scaffolds was assessed using the ethanol immersion method in a specific gravity bottle, following the procedure outlined in a previous study [30]. Porosity measurements were conducted on scaffolds with different line spacings (ranging from 1.0, 1.2, 1.4, 1.6, 1.8, 2.0, 2.2, 2.4, 2.6, 2.8, and 3.0 mm) with three samples analyzed per spacing group.

Swelling and hydration of the scaffolds were determined using a weighing method. The scaffolds produced by 3D bioprinting were first freeze-dried, and their dry weight (W_0) was measured. Subsequently, these freeze-dried scaffolds were immersed in deionized water at 37 °C to enable swelling. At five-hour intervals, the scaffolds were removed from the water, the surface moisture was wiped off, and the weight (W_t) was measured. This process was repeated until the scaffolds reached a swelling equilibrium. The mass of the scaffold at this point was recorded as W_1. The dynamic swelling ratio (DSR) and balanced water content (BWC) of the scaffolds were calculated using the following formulas (n = 3): $DSR = (W_t - W_0)/W_0$ and $BWC = (W_1 - W_0)/W_1$.

The scaffolds containing BMSCs printed with different printing lines spacings were transferred to a 24-well plate and cultured in DMEM with 10% FBS. On the third day, cell proliferation was assessed using a CCK-8 assay kit.

The mechanical properties of the scaffolds were characterized using a rheometer (Thermo Scientific HAAKE MARS60, USA) to measure the storage modulus (G') and loss modulus (G'') of different scaffolds under dynamic strain scanning mode at 37 °C.

A digital camera (Nikon, Japan) was used to capture macroscopic images of the scaffold. The scaffolds were then dehydrated using a freeze dryer (Labconco FreeZone, USA). After fracturing the scaffold in liquid nitrogen, it was coated using a gold jet machine (JEOL JEC-3000FC, Japan) to enhance its conductivity. Subsequently, the scaffold was observed under a SEM (JEOL JSM-IT800, Japan) to examine its surface and cross-sectional structures, providing insights into the morphological features and the uniformity of the scaffold structure.

The biocompatibility of the scaffold was assessed using live/dead staining. Chondrogenic organoids were cultured in DMEM (with 10% FBS and 1% $CaCl_2$). The medium was changed every three days to maintain nutrient availability and waste removal. Live/dead staining was performed on the first, third, and seventh days to evaluate cell viability within the scaffold. Stained cells were imaged using a laser-scanning confocal microscope (Nikon A1, Japan), which enabled high-resolution visualization of live (typically stained green) and dead (typically stained red) cells within the organoids.

Further, the same batch of MNP-BMSCs was divided into two groups for experimental comparison. One portion was seeded at a concentration of 10^6 cells in 10 cm cell culture dishes for a conventional two-dimensional (2D) culture. The other portion was mixed with the hydrogel, adjusted to the same cell concentration, and bioprinted into organoids for a 3D culture environment. Both sets of MNP-BMSCs underwent chondrogenic differentiation. Samples were collected on the third day post differentiation, and total RNA was extracted after cryogenic grinding to preserve RNA integrity. On the seventh day post differentiation, samples were collected again, and both total RNA and total protein were extracted using the same method. Real-time quantitative polymerase chain reaction (RT-qPCR) and Western blot analyses were performed to quantitatively assess gene and protein expression levels, respectively.

Using the identical bioink, two distinct organoid types were constructed via 3D bioprinting and syringe extrusion methods. After seven days of chondrogenic differentiation, longitudinal sections of both organoid types were stained with Safranin-O.

To assess whether the shell of the mixed hydrogel can restrict cells to grow and differentiate within the scaffold, we designed relevant experiments. Utilizing a 3D bioprinter, a dual-layered model structure was fabricated. The upper layer comprised bio-ink mixed with MNP-BMSCs, while the lower layer consisted solely of hydrogel material. Each layer measured 2 mm in thickness. In the post-crosslinking stacked model, a layer of hydrogel material was printed and cross-linked with 5% $CaCl_2$. Subsequently, bioink was deposited onto this base and cross-linked. Conversely, the hydrogel was first printed in the pre-crosslinked stacked model, followed by bioink application; the entire structure was then cross-linked with 5% $CaCl_2$.

2.8 Construction of *in vitro* cartilage organoids

BMSCs, chondrocytes, and MNP-BMSCs were each mixed with an alginate-gelatin bioink to fabricate organoids using a 3D bioprinter. The organoids derived from BMSCs and MNP-BMSCs were cultured in a chondrogenic differentiation medium, whereas those from chondrocytes were maintained in DMEM (with 10% FBS and 1% $CaCl_2$). Proteins Col-II and Aggrecan were stained using standard immunofluorescence techniques and visualized with a confocal laser scanning microscope (Nikon A1, Japan). Total protein from each scaffold was extracted using radio-immunoprecipitation assay (RIPA) cell/tissue lysis buffer, which included a protease inhibitor cocktail. The target proteins were

transferred to a polyvinylidene fluoride (PVDF) membrane following sodium dodecyl sulfate-polyacrylamide gel electrophoresis (SDS-PAGE) (Bio-Rad PowerPac, USA). This membrane was blocked with a blocking solution for 1 h, followed by overnight incubation at 4 °C with rabbit anti-Col-II and anti-Aggrecan antibodies. Subsequently, the membranes were incubated with goat anti-rabbit IgG horseradish peroxidase (HRP) secondary antibodies at room temperature for 2 h, and detection was carried out using an enhanced chemiluminescence system (Cytiva ImageQuant 800, USA).

For the mechanical evaluation of the three types of organoids, cubic organoids with a side length of 2 cm and height of 4 mm were 3D bioprinted. After 14 days of chondrogenic culture, the compressive modulus was measured using a universal material testing machine (Instron 68SC-1, USA).

2.9 *In vivo* cartilage defect repair with the organoids

All SD rats (6 weeks, male) utilized in this study were acquired from the Experimental Animal Center of Central South University (XMSB-2023-0061). The experimental protocol received approval from the same institution. The animal experimental groups included sham surgery, control, scaffold, MNP-BMSCs, and organoid groups.

The rats were anesthetized using an animal gas anesthesia machine (RWD R640, China). A cartilage defect model was created in the central region of the femoral condyle, measuring 2 mm in diameter and 1.5 mm in depth, using a sterile skin puncher (2 mm). Cylindrical implants were harvested at the intersection of the ink in the cartilage-differentiated organoids and cell-free scaffolds. The scaffold and organoid groups had these implants placed into the defect sites, followed by wound closure. In the MNP-BMSC group, 1×10^5 cartilage-differentiated MNP-BMSCs were injected into the joint cavity post-wound closure. Following wound closure, the surgical areas of all animals were disinfected, and comprehensive postoperative care, including antibiotics and pain management, was administered. At 4 and 8 weeks post operation, the animals were euthanized, and samples from their femurs, hearts, livers, spleens, lungs, kidneys, and left ventricular blood were collected for analysis. All tissues were fixed in 4% paraformaldehyde, and macroscopic photographs were captured. Following femoral tissue decalcification, 5-micrometer-thick paraffin sections were prepared using an automated paraffin microtome (Leica Autocut, Germany). These sections underwent hematoxylin-eosin (HE), Safranin-O/Fast green, and Sirius red staining using an automated staining machine (Sakura DRS-Prisma-P-CNS, Japan). Immunohistochemistry was performed to detect Col-II and Aggrecan expression in the defect area. ImageJ software facilitated the quantitative analysis of the immunohistochemical staining. Heart, liver, spleen, lung, and kidney tissues were processed similarly for HE staining. Blood samples were analyzed using a blood analyzer (Sysmex XN1000V, Japan) and a biochemical analyzer (Hitachi 7180, Japan) to assess *in vivo* biocompatibility.

2.10 Statistical analysis

The experimental data were obtained from a minimum of three independent experiments and are presented as mean ± standard deviation. Group comparisons were performed using the *t*-test for pairwise comparisons and one-way analysis of variance (ANOVA) for multiple comparisons. Statistical significance was set at p of less than 0.05.

3 Results

3.1 Morphology and characterization of the magnetic nanoparticles

Magnetic nanoparticles, particularly magnetite (Fe_3O_4), exhibit excellent biocompatibility and are widely used to construct engineered cells [31]. A TEM study of the magnetite nanoparticles used in the experiment (Fig. 1(a)), revealed that the nanoparticles mostly exhibited irregular shapes. SEM and energy-dispersive spectroscopy (EDS) analysis revealed that the nanoparticles were composed of magnetite (Figs. 1(b) and 1(c)). No other elements were detected in the spectroscopic images, indicating the high purity of the particles. The magnetism of the nanoparticles was evaluated using a VSM. The magnetic hysteresis loop of the MNPs indicated their superparamagnetic nature (Fig. 1(d)). Multiple studies have indicated that the optimal diameter for nanoparticles to be internalized by cells is 25–30 nm [32, 33]. Dynamic light scattering (DLS) used to assess the size of the nanoparticles indicated that majority of MNPs are distributed around 25.54 nm in diameter (Fig. 1(e)). Subsequently, we evaluated the biocompatibility of the MNPs using rat BMSCs. The CCK-8 assay indicated no significant difference in the proliferation capacity of BMSCs when co-cultured with a medium containing different concentrations of MNPs (10, 50, 100, and 150 μg/mL) after 24 h (Fig. 1(f)). Subsequently, we further clarified the IC50 of MNPs on rat BMSCs using the CCK-8 assay, and the results indicated that the IC50 was 901.6 μmol (Fig. S1(a) in the Electronic Supplementary Material (ESM)). BMSCs co-cultured with different concentrations of MNPs were subjected to live/dead, EdU, and phalloidin staining to further assess cell viability, proliferation capacity, and cell morphology (Figs. 1(g)–1(k)). The results indicated no significant signs of cell death, inhibition of proliferation, or changes in the cytoskeleton. This study defined BMSCs that took up MNPs as engineered MNP-BMSCs. To further investigate the internalization efficiency of MNPs and the optimal time point for constructing MNP-BMSCs, we co-cultured BMSCs in DMEM (with 10% FBS) containing 150 μg/mL MNPs. At different time points (0.5, 1, 2, 4, 8, 12, and 24 h), the BMSCs were collected and subjected to Prussian blue staining and TEM imaging (Fig. 1(l)). The results indicated that after 12 h, most BMSCs exhibited uptake of MNPs within their interior. Therefore, all engineered MNP-BMSCs in the experiments were constructed using this protocol.

3.2 The impact of MNPs on the polarity of BMSCs

Planar cell polarity is crucial for normal cell growth, morphogenesis, and functionality [34–36]. To investigate the effect of the magnetic MNPs on the polarity of BMSCs, we labeled the GM-130 marker of the endoplasmic reticulum with fluorescent antibodies (AF-488) to act as a polarity complex. This complex indirectly assesses the distribution of organelles within the cell, reflecting cell polarity (Fig. 2(a)). The results indicated that, compared to the control group, MNPs-BMSCs exhibited significant cell polarity, with the endoplasmic reticulum clustered on one side of the nucleus. In contrast, the endoplasmic reticulum was uniformly distributed around the nucleus in the control group. Subsequently, we assessed the cell polarity of multicellular fields and quantified the direction of cell polarity (Fig. 2(b)). The results showed a significant increase in the number of polarized cells in the MNPs-BMSC group compared to the control group. Additionally, in the MNPs-BMSC group, the direction of cell polarity was

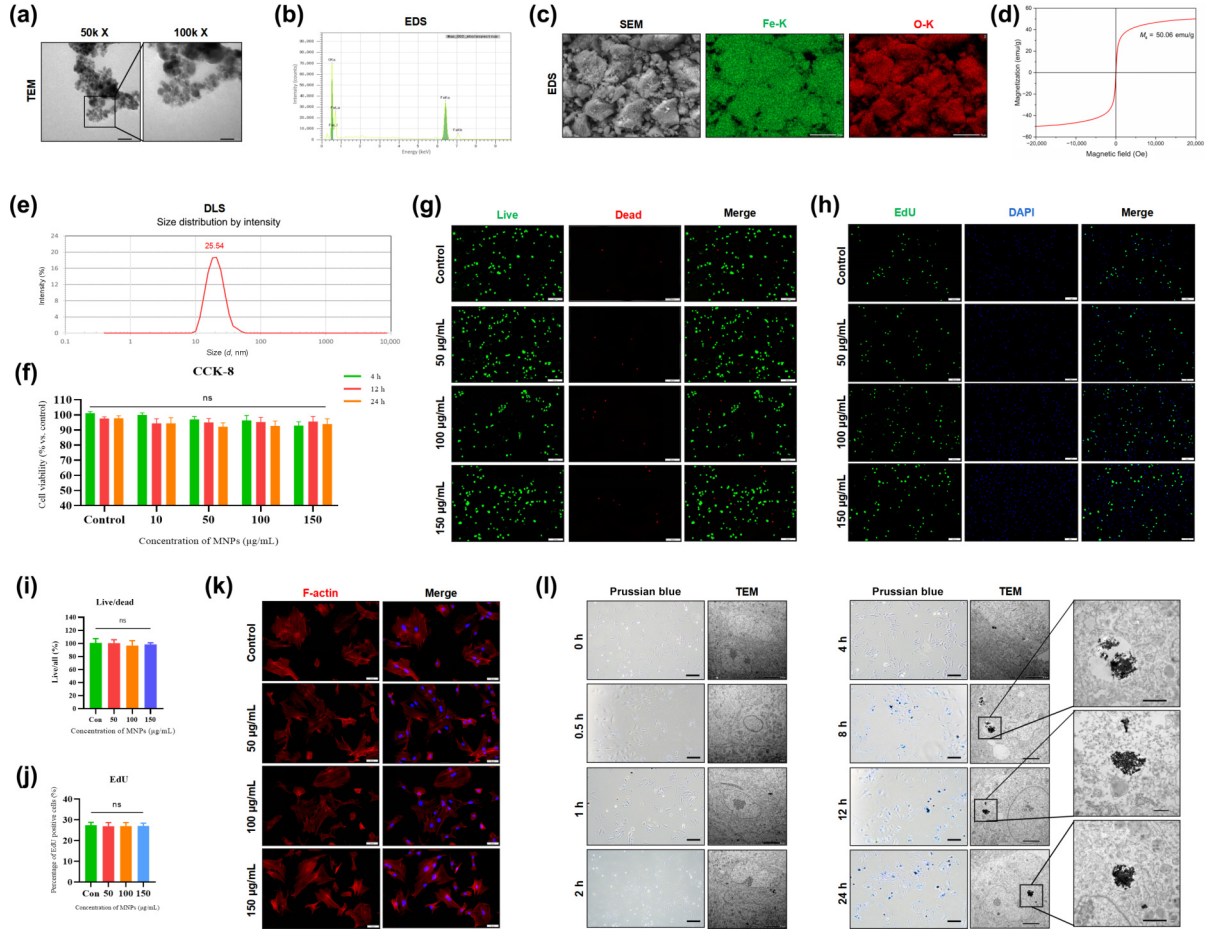

Figure 1 Morphology and characterization of the magnetic nanoparticles. (a) TEM images of the MNPs. (b) and (c) EDS analysis of the MNPs with SEM. (d) Field-dependent hysteresis loops of the nanoparticles. (e) Size distribution of the MNPs measured by DLS. (f) Relative cell viability of BMSCs after co-cultured with 10, 50, 100 and 150 μg/mL MNPs for 24 h (n = 3). (g) Live/dead (n = 3) and (h) EdU staining images (n = 3) of BMSCs co-cultured with 50, 100 and 150 μg/mL MNPs for 3 days (scale bars 200 μm). (i) and (j) Statistical analysis of Live/dead and EdU staining. (k) F-actin staining images of BMSCs co-cultured with 50, 100 and 150 μg/mL MNPs for 3 days (scale bars 50 μm). (l) Prussian blue staining and TEM imaging of BMSCs co-cultured with 150 μg/mL MNPs at 0.5, 1, 2, 4, 8, 12 and 24 h (scale bars (100 μm, Prussian blue), (5 and 2 μm, TEM)).

primarily distributed between 210° and 330°, whereas in the control group, it was uniformly distributed from 0° to 360°. To clarify whether the polarity of MNPs-BMSCs can be maintained, we further examined the cell polarity 7 days after the successful construction of MNPs-BMSCs and after passage (Fig. 2(c)). The results confirmed that the cell polarity was not affected by culture time or passage.

To further explore the potential reasons for the change in cell polarity induced by MNPs in BMSCs, we collected both MNP-BMSCs and control BMSCs and extracted total RNA for transcriptomic analysis (mRNA-seq). Principal component analysis was used to compare the gene expression patterns between the control (BMSCs) and experiment (MNPs-BMSCs) groups (Fig. 2(d)). The comprehensive analysis identified 1096 DEGs, with 585 downregulated and 511 upregulated (Fig. 2(e)).

Further analysis was conducted using volcano plots and clustered heat maps to illustrate the DEGs in each group (Figs. 2(f) and 2(g)). GO analysis divided these genes into three main categories: biological processes, molecular functions, and cellular components (Fig. 2(h)). Compared to the control group, the MNPs-BMSC group exhibited upregulation in several biological processes, including cell communication, extracellular matrix organization, anatomical structure morphogenesis, signal transduction, movement of cell or subcellular component, and cell adhesion. These processes are all associated with cell polarity. In molecular functions, the upregulated functions include cell adhesion molecule binding, cytoskeletal protein binding, cytoskeletal motor activity, and signaling receptor binding, all related to cell polarity. Additionally, glycosaminoglycan and collagen binding are associated with the chondrogenic differentiation of BMSC. In cellular components, the upregulated elements include the extracellular matrix, external encapsulating structure, cell junction, plasma membrane, anchoring junction, and actin cytoskeleton, all integral to cell polarity. Moreover, the collagen-containing extracellular matrix and the extracellular region are associated with the chondrogenic differentiation of BMSC.

The KEGG pathway enrichment analysis further elucidated the functions of the DEGs (Fig. 2(i)). Compared to the control group, the MNPs-BMSC group exhibited upregulation in the top three KEGG enrichments: ECM–receptor interaction, regulation of actin cytoskeleton, and focal adhesion, all strongly related to cell polarity. The results of the GSEA are displayed in Fig. 2(j). Collectively, the findings from the GO, KEGG, and GSEA indicate that MNPs significantly upregulated genes associated with cell polarity, cell adhesion, motility, cytoskeletal changes, and chondrogenic differentiation. Alterations in cell polarity influence cellular

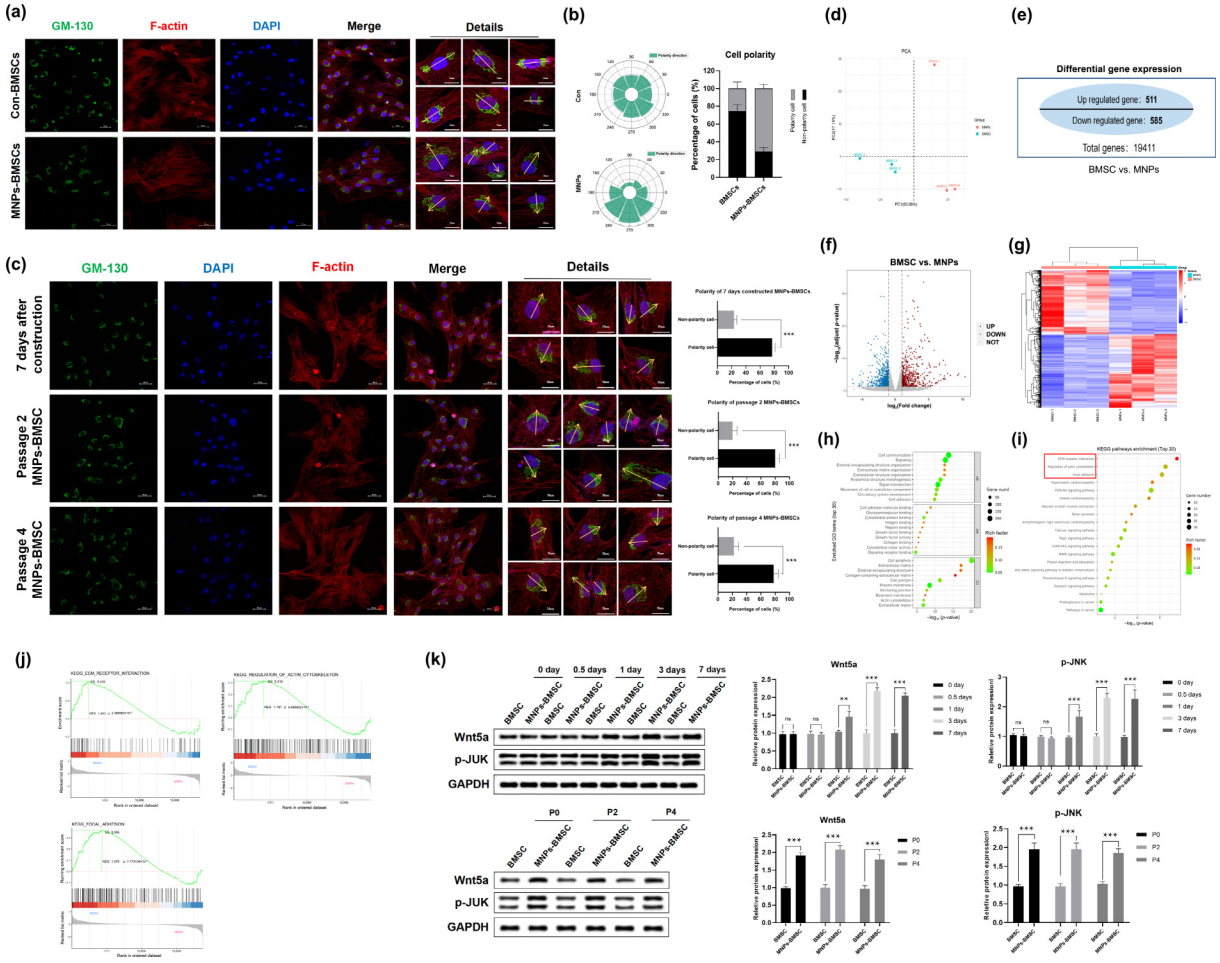

Figure 2 The impact of MNPs on the polarity of BMSCs. (a) Immunofluorescence images of GM-130 and F-actin on BMSCs and MNPs-BMSCs (scale bars 50 and 20 μm). (b) Cell polarity analysis of BMSCs and MNPs-BMSCs (n = 8). (c) Effects of long-term culture and passaging on the cell polarity of MNPs-BMSCs (n = 8). (d) PCA of DEGs distributed in the BMSC group (blank) and MNPs group (MNPs-BMSCs). (e) Comparative assessment of mRNA expression in the BMSC group and MNPs group. (f) Volcano plot representation of genes exhibiting significant expression changes exceeding a 2-fold difference in transcriptome sequencing results. (g) Heatmap of gene expression clustering for DEGs. (h) GO and (i) KEGG analysis for upregulated genes in MNP group. (j) GSEA enrichment analysis for ECM receptor interaction pathway, regulation of actin cytoskeleton pathway and focal adhesion pathway in BMSCs. (k) Activation of the Wnt-PCP signaling pathway in cells at different time points after MNPs-BMSC construction and passaging cells.

functions, including cell migration and chondrogenic differentiation, providing reliable evidence for further research.

Since the Wnt-PCP signaling pathway is a key signaling pathway that directly affects cell polarity, we further investigated whether MNPs induce polarization of BMSCs by activating the Wnt-PCP signaling pathway. We studied the activation of the Wnt-PCP signaling pathway at different time points (0, 0.5, 1, 3, and 7 days) and after passage (P2 and P4) in cells following the successful construction of MNPs-BMSCs using Western Blot (Fig. 2(k)). The results indicated that the Wnt-PCP signaling pathway was activated one day after the successful construction of MNPs-BMSCs, with activation levels significantly increasing over time. Additionally, significant Wnt-PCP signaling pathway activation was still observed in MNPs-BMSCs after passage.

3.3 Promotion of the chondrogenic differentiation of BMSCs by MNPs

Following transcriptomic analysis, we observed that MNP-BMSCs exhibited enhanced cell polarity, cell motility, and chondrogenic differentiation compared to the control group of BMSCs. Consequently, we investigated the impact of MNPs on the chondrogenic differentiation of BMSCs. Initially, results from the Transwell indicated a significant increase in the invasiveness of MNPs-BMSCs relative to the control group (Fig. 3(a)). Additionally, the scratch test demonstrated a marked enhancement in the migration capability of MNPs-BMSCs (Fig. 3(b)).

We then compared the chondrogenic differentiation abilities of MNP-BMSCs and control BMSCs. We utilized reverse transcription quantitative RT-qPCR to analyze the expression of chondrogenic-associated cell markers during the chondrogenic differentiation process, including Type I collagen (Col-I), Type II collagen (Col-II), Type X collagen (Col-X) and Aggrecan (ACAN) (Fig. 3(c)). Compared to the BMSC group, MNP-BMSCs showed differential upregulation of Col-II, Col-X, and Aggrecan genes by the third day of chondrogenic differentiation. By the seventh day, Col-II and Aggrecan exhibited significantly higher expression levels in the MNP-BMSC group, whereas Col-X expression displayed a decreasing trend. This indicates that MNPs primarily promote the upregulation of cartilage-specific genes during the chondrogenic differentiation of BMSCs, with limited promotion of fibrocartilage and inhibitory effects on chondrocyte hypertrophy.

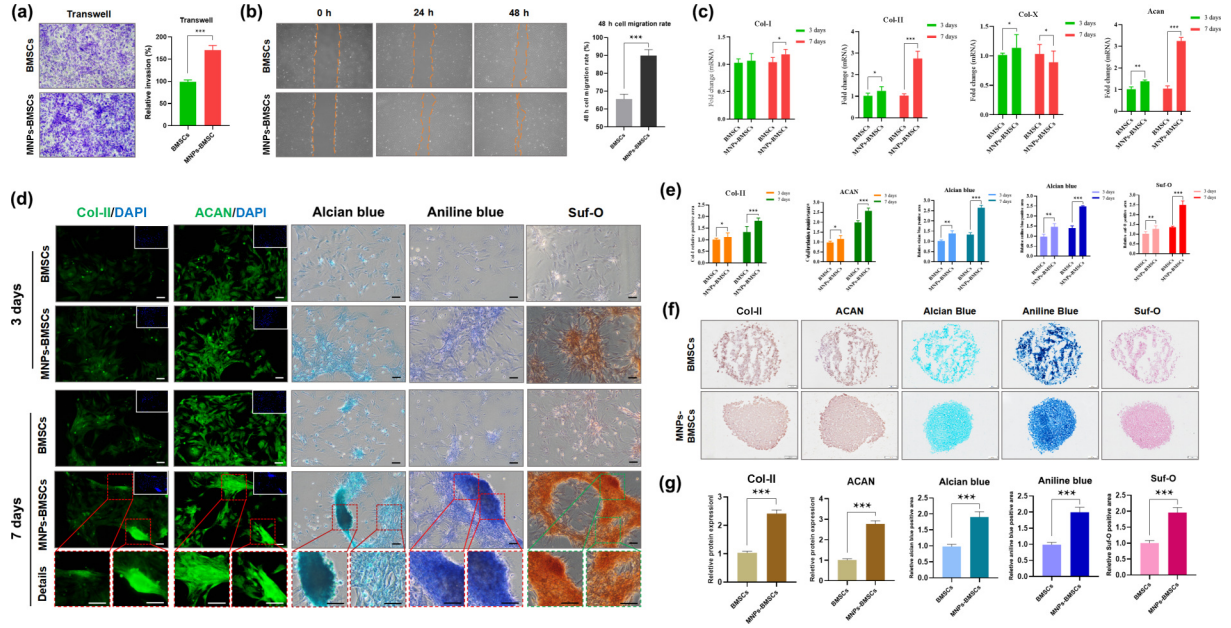

Figure 3 MNPs promote the chondrogenic differentiation of BMSCs. (a) Transwell (n = 3) and (b) scratch test (n = 3) of BMSCs and MNPs-BMSCs (scale bars 100 μm). (c) The gene expression of cartilage-related markers including Col-I, Col-II, Col-X and Acan (n = 3). (d) Immunofluorescence images of Col-II, ACAN, Alcian blue, Aniline blue and Safranin-O staining of BMSCs and MNPs-BMSCs after 3 and 7 days of chondrogenic differentiation (scale bars 100 μm) and (e) statistical analysis (n = 3). (f) Immunochemistry images of Col-II, ACAN, Alcian Blue, Aniline Blue and Safranin-O staining of chondrogenic pellet culture on BMSCs and MNPs-BMSCs after 14 days of chondrogenic differentiation (scale bars 100 μm) and (g) statistical analysis (n = 3).

Further, immunofluorescence staining was used to detect Col-II and Aggrecan expression in the two cell types undergoing chondrogenic differentiation. Additionally, Alcian blue, aniline blue, and Safranin-O staining were employed to assess the level of chondrogenic differentiation in all BMSCs (Figs. 3(d) and 3(e)). On the third day, there were no significant differences in the expression of Col-II and Aggrecan between the two groups, nor was there any intensity of the three stains. By the seventh day, compared to that in the control group, the expression of Col-II and Aggrecan in the MNPs-BMSCs group had significantly increased, with a noticeable enhancement in the intensity of all three stains. Similarly, MNP-BMSCs exhibited significant aggregation during differentiation, forming numerous cell clusters with significantly higher expression of Col-II and Aggrecan proteins. All three stains showed abundant collagen and glycosaminoglycans within these aggregated cell clusters, a phenomenon not observed in the control group.

In addition to the analysis of 2D chondrogenic differentiation, we investigated the differences in chondrogenic differentiation of the two cell types in 3D chondrogenic spheres in the presence of MNPs. After 14 days of chondrogenic differentiation with chondrogenic pellet culture, we conducted protein expression and structural analysis within the spheres, including analyses of the expression of Col-II and Aggrecan proteins, as well as Alcian blue, aniline blue, and Safranin-O staining (Figs. 3(f) and 3(g)). There was no significant difference in the expression of Col-II and Aggrecan between the two types of chondrogenic spheres. Similarly, there was no significant difference in the three types of staining. However, compared to the chondrogenic spheres formed by the control BMSCs, the structure of the MNPs-BMSCs was denser, with the control group's spheres appearing loose and exhibiting noticeable internal cracks. In summary, it has been suggested that the MNPs enhances the ability for BMSCs aggregation, intercellular communication, and cell adhesion, all of which are conducive to the chondrogenic differentiation of BMSCs.

To further investigate the effect of MNPs on BMSC differentiation, we induced osteogenic differentiation (Fig. S1(b) in the ESM). The results indicated that after 7 days of osteogenic differentiation, the MNPs-BMSC group formed more calcium nodules compared to the control BMSC group, and the expression of alkaline phosphatase (ALP) significantly increased, confirming that their osteogenic differentiation ability was also significantly enhanced. Regarding whether MNPs would cause BMSCs to differentiate in a non-inductive environment, we used flow cytometry to assess the successfully constructed MNPs-BMSCs at different time points (Fig. S1(c) in the ESM). The results showed that MNPs do not induce unintended or nonspecific differentiation in a non-inductive environment.

3.4 Construction of engineered magnetic nanoparticles polarized-BMSCs/alginate/gelatin cartilage organoids

Gelatin, a denatured, water-soluble polypeptide derived from the irreversible hydrolysis of collagen, is one of the most crucial components of cartilage [37]. The collagen breakdown into gelatin disrupts its triple-helical structure, resulting in three peptide chains. This process renders the material biocompatible and biodegradable, facilitating cell growth [38]. Alginate, a commonly used natural biopolymer, is known for its biocompatibility, biodegradability, non-antigenicity, chelating ability, and excellent long-term stability [39]. Therefore, we utilized a composite hydrogel composed of gelatin and alginate as a scaffold for the organoids. Leveraging the low-temperature gelation property of gelatin facilitated the 3D bioprinting process. The stability of the scaffold during the cultivation process was ensured by the ion cross-linking of alginate (Fig. 4(a)). While gelatin remains in a sol state at 37 °C, primarily providing support during the printing process, the mechanical properties of the scaffold during organoid cultivation are mainly provided by the cross-linked alginate.

Therefore, it is crucial to ensure a high alginate content in the

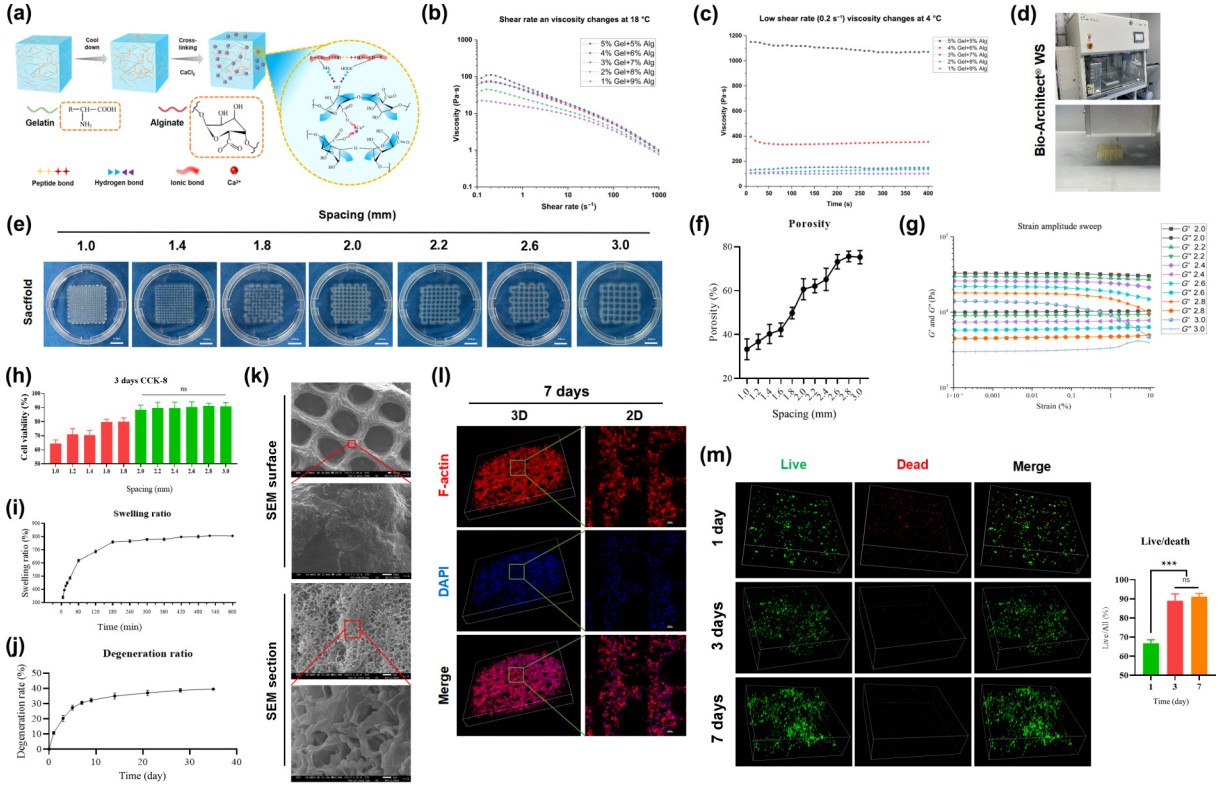

Figure 4 Construction of engineered MNPs-BMSCs/alginate/gelatin cartilage organoids. (a) The crosslinking principle of alginate and gelatin mixed hydrogels. (b) Viscosity test of different ratios of alginate and gelatin mixed hydrogels at 37 °C. (c) Extremely low shear rates viscosity test of different ratios of alginate and gelatin mixed hydrogels at 4 °C. (d) 3D bioprinter and printing process. (e) Images of hydrogel scaffolds with different printing spacings (scale bars 0.5 cm). (f) Statistics porosity of different scaffolds (n = 3). (g) Storage modulus (G') and loss modulus (G'') of different scaffolds. (h) 3 days cell proliferation of hydrogels containing BMSCs as bio-ink to construct different scaffolds (n = 3). (i) Statistics porosity of 5% alg + 5% gel hydrogel scaffold (n = 3). (j) Degradation performance of 5% alg + 5% gel hydrogel scaffold *in vitro* (n = 3). (k) SEM images of surface and section of 5% alg + 5% gel hydrogel scaffold. (l) Red phalloidin staining images of 3D bioprinted MNPs-BMSCs/alginate/gelatin cartilage organoids at 7 days. (m) Live/dead staining images of 3D bioprinted MNPs-BMSCs/alginate/gelatin cartilage organoids at 1, 3 and 7 days (n = 3).

scaffold while maintaining as low a gelatin content as possible to preserve a printable state. We experimented with various ratios of mixed gels and confirmed that a combination of 5% alginate and 5% gelatin is most suitable (Figs. 4(b) and 4(c)). This hydrogel maintains low viscosity under high shear stress, facilitating smooth extrusion through the printing nozzle at 18 °C. Conversely, when tested at 4 °C under extremely low shear rates to simulate static conditions, this hydrogel exhibited high viscosity, ensuring the stability of the printed scaffold structure before cross-linking. The printed model featured a cross-shaped cubic structure, with the longitudinal distribution of the bio-ink primarily aimed at simulating the middle layer structure of the cartilage. Utilizing the low-temperature mode of the 3D bioprinter enabled the construction of the entire organoid (Fig. 4(d)).

Subsequently, we prepared multiple organoid scaffolds using different printing spacings (Fig. 4(e)) and measured their porosity (Fig. 4(f)), storage modulus (G'), and loss modulus (G'') (Fig. 4(g)) individually. We used a bio-ink containing mixed BMSCs to prepare multiple organoids with different printing spacings. Cell viability was measured after three days of culture using the CCK-8 assay (Fig. 4(h)). The printing spacing was directly proportional to the scaffold porosity, affecting the cell growth and differentiation. Higher porosity facilitates better nutrient and oxygen diffusion into the cells. When the printing spacing exceeded 2 mm, there was no significant difference in cell survival within the scaffold. Additionally, G' and G'' reflect the mechanical properties of the scaffold, with the results indicating an inverse relationship between mechanical performance and printing spacing. Considering these findings, we selected a printing spacing of 2 mm for further experiments. Subsequently, we measured the swelling and *in vitro* degradation rates of the scaffolds in simulated body fluid (Figs. 4(i) and 4(j)). The scaffold rapidly absorbed water within the first 180 min, followed by a slower absorption rate, reaching swelling equilibrium after 420 min. In the *in vitro* degradation experiment, the degradation rate was relatively rapid during the first three days, decreased by the fifth day, and reached 38.8% by the 35th day. This pattern indicated that the internal structure of the scaffold was adequately cross-linked, stable, and exhibited a relatively slow overall degradation rate. SEM was used to characterize the surface and internal structures of the scaffolds (Fig. 4(k)). The surface of the scaffold appeared smooth with no significant pore structures, whereas the internal structure was loose and porous. This internal structure offers advantages for cell growth, migration, and differentiation within the scaffold, whereas the smooth surface layer helps confine cells within the scaffold, enhancing cell utilization. Organoids were constructed using a mixed MNPs-BMSCs bio-ink; the biocompatibility of the scaffold was assessed using F-actin and live/dead staining (Figs. 4(l) and 4(m)). Cytoskeletal imaging showed that MNPs-BMSCs spread out within the scaffold, with normal cytoskeletal structure, confirming that the 3D bioprinted alginate/gelatin scaffold is suitable for cell growth. Many dead cells were observed within the scaffolds on the first day after printing.

However, by the third and seventh day after culturing, the proportion of dead cells significantly decreased, and the number of live cells increased.

3.5 *In vitro* evaluation of the advanced cartilage organoids

To investigate the differences in chondrogenic differentiation of MNPs-BMSCs in 2D (flat culture) and 3D (organoid) environments, we used RT-qPCR to evaluate the expression of chondrogenic differentiation-related genes after 3 and 7 days (Fig. 5(a)). Western blotting was performed to assess the expression of related proteins on the seventh day (Fig. 5(b)). The results showed that the expression levels of Aggrecan and Col-II genes and proteins were significantly higher in organoid cultures than in 2D cultures. To explore the advantages of 3D bioprinting in constructing cartilage organoids, we used the same bio-ink to create two types of cartilage organoids: one using 3D bioprinting and the other using simple extrusion with a syringe. After seven days of chondrogenic differentiation, longitudinal sections of both cartilage organoids were stained with Safranin-O (Fig. 5(c)). Cartilage organoids constructed using 3D bioprinting exhibited denser structures than those created by syringe extrusion. Collagen fibers were interwoven within the hydrogel structure, primarily extending longitudinally, which better simulated the middle layer of cartilage.

Furthermore, to investigate the restriction of cells by the surface layer of the organoids, we first used SEM to observe their morphology (Fig. 5(d)). The surface of the organoids constructed using 3D bioprinting formed a thin, low-porosity layer, whereas the interior maintained a loose, porous structure. This design effectively restricts cell growth, division, and differentiation within the interior of the organoids, which in turn improves the efficiency of cell utilization. To further investigate the restrictive effect of the surface layer on cells, we constructed two types of organoids using post- and pre-crosslinking stacking. After seven days of chondrogenic differentiation, phalloidin staining was used to observe cell migration and distribution (Fig. 5(e)). In the pre-crosslinked stacked organoids, the cells predominantly exhibited an elongated spindle shape and crossed the stacking interfaces freely, indicating their ability to move within the organoids. Conversely, in the post-crosslinking stacked organoids, the cells could not penetrate the hydrogel surface layer formed by cross-linking, demonstrating the restrictive effect of the organoid surface layer on cell movement.

To identify the optimal seed cells for constructing *in vitro* cartilage organoids, we used chondrocytes, BMSCs, and MNP-BMSCs as seed cells to create three cartilage organoids. The chondrocyte group was conventionally cultured, whereas the BMSC and MNP-BMSC groups underwent chondrogenic differentiation. After seven days of culture, the expression levels of Col-II and Aggrecan in the three types of cartilage organoids were preliminarily assessed using RT-qPCR (Fig. 5(f)). Subsequently, total protein was extracted from the scaffolds, and Western blot analysis was performed to compare the protein expression of Col-II and Aggrecan in the three types of cartilage organoids (Fig. 5(g)). Both methods confirmed a significant increase in the expression of cartilage-related proteins in the MNP-BMSC group compared with the other two groups. This preliminary study suggests that MNP-BMSCs are optimal seed cells for constructing *in vitro* cartilage

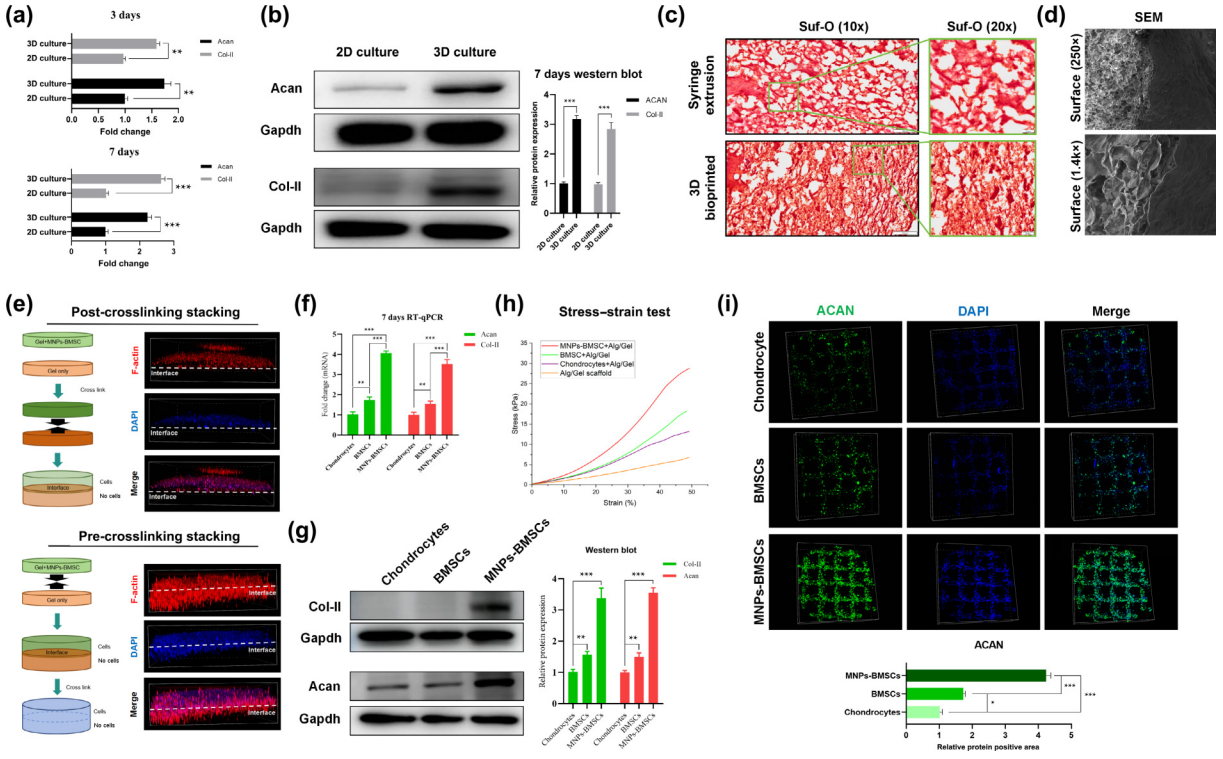

Figure 5 *In vitro* evaluation of the advanced cartilage organoids. (a) The gene expression of Col-II and Acan in 2D and 3D cultured MNPs-BMSCs at 3 and 7 days (n = 3). (b) Representative Western blot results of Col-II and ACAN in 2D and 3D cultured MNPs-BMSCs at 7 days (n = 3). (c) Safranin-O staining of the longitudinal sections in 3D bioprinted and syringe extrusion cartilage organoids (scale bars 200 and 50 μm). (d) SEM images of the surface section of the organoid. (e) Testing for cell restriction by organoid surface layers. (f) The gene expression of Col-II and Acan in three types of seed cells (chondrocytes, BMSCs and MNPs-BMSCs) constructed cartilage organoids at 3 and 7 days (n = 3). (g) The protein expression of Col-II, ACAN in 3 types of cartilage organoids at 7 days cultured (n = 3). (h) Stress–strain curves of 3 types of cartilage organoids at 7 days cultured. (i) 3D reconstruction immunofluorescence images of ACAN in 3 types of cartilage organoids at 7 days cultured (n = 3).

organoids. As for the mechanical properties of the three types of cartilage organoids, primarily focusing on their ability to withstand compressive deformation. The results are presented as stress–strain curves (Fig. 5(h)). First, compared with the cell-free scaffold, all three types of cartilage organoids demonstrated improved resistance to compressive deformation. Second, within the 0%–35% strain range, the chondrocyte and BMSC groups exhibited similar compressive resistance. However, in the 35%–50% strain range, the BMSC group performed better. The MNP-BMSC group displayed significantly enhanced compressive resistance across the 0%–50% strain range, particularly at 50%. Further characterization was performed using immunofluorescence to visualize the expression of Aggrecan in organoids after 7 days of culture, followed by 3D reconstruction imaging to determine the spatial distribution of these proteins (Fig. 5(i)). In the MNPs-BMSC group, a large number of stem cells were observed to undergo self-assembly, forming multiple irregularly shaped chondrocyte aggregates. These aggregates expressed high levels of aggrecan proteins both inside and around them. Although aggrecan expression was also observed in the chondrocyte and BMSC groups, the cells in the scaffold predominantly existed as single entities, lacking the conditions necessary to form cartilage organoids. These findings indicate that MNP-BMSCs are optimal seed cells for constructing cartilage organoids.

3.6 *In vivo* cartilage defect repaired by the cartilage organoids

To assess the ability of cartilage organoids constructed using MNP-BMSCs to regenerate cartilage *in vivo*, we utilized a standard rat articular cartilage defect model (2 mm × 1.5 mm). The experimental animals were randomly assigned to five groups, as shown in Fig. 6(a): Sham group (positive control), control group (untreated group), scaffold group (treated with a scaffold made of alginate and gelatin only), cell injection group (treated with intra-articular injection of MNP-BMSCs only), and cartilage organoids group (treatment group receiving cartilage organoids). At 4- and 8-weeks post-surgery, the rats were euthanized, and tissue specimens from the femur, heart, liver, spleen, lungs, and kidneys were collected for subsequent analysis.

The cartilage defect at the distal end of the femur was evaluated macroscopically (Fig. 6(b)). Compared to the control group, the scaffold, MNP-BMSC injection, and cartilage organoid groups recovered at the cartilage defect position. However, the cartilage organoid group exhibited the most significant restoration, with the cartilage tissue appearing filled and smooth, closely resembling the normal cartilage of the sham group. Subsequently, macroscopic evaluations were conducted according to the standards of the International Cartilage Repair Society (Fig. 6(c)).

To further evaluate the repair of cartilage defects, animal samples

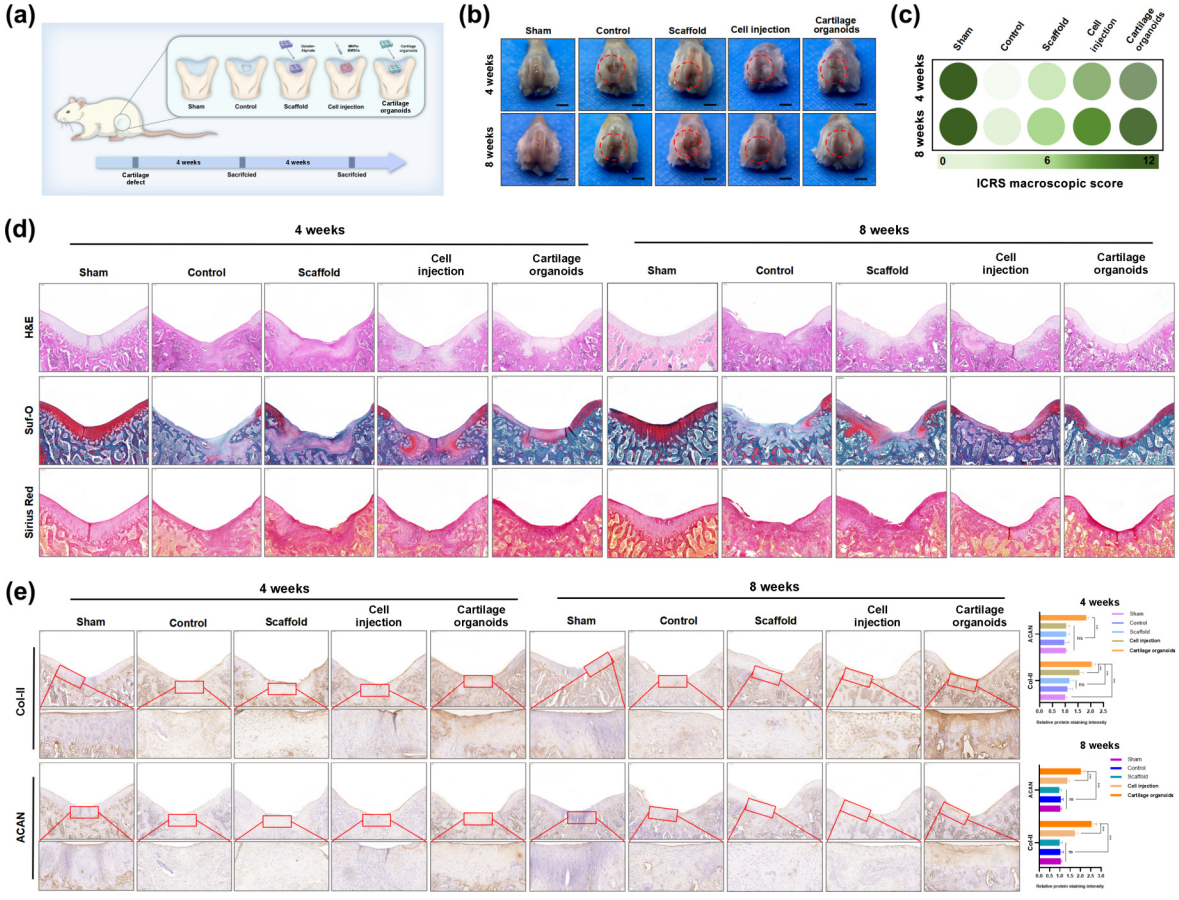

Figure 6 *In vivo* cartilage defect repaired by the cartilage organoids. (a) Scheme of cartilage defect modeling and treatment protocol. (b) Gross observation of femur cartilage after treatment at 4 and 8 weeks (scale bars 2 mm). (c) Heat map of ICRS macroscopic assessment of cartilage at 4 and 8 weeks (n = 3). (d) Representative H&E, Safranin-O/Fast Green and Sirius Red staining of femur cartilage at 4 and 8 weeks after treatment (scale bars 0.1 mm). (e) Immunohistochemical staining and Quantitative analysis of Col-II and ACAN in rat cartilage post-treatment defects (scale bars 0.1 and 0.05 mm) (n = 3).

were prepared as paraffin-embedded tissue sections and stained with Hematoxylin and Eosin (H&E), Safranin-O/Fast Green (Saf-O), and Sirius Red (Fig. 6(d)). In the fourth week post operation, HE and Saf-O staining results indicated significant damage to the cartilage layer in the control group compared to that in the sham group. The damaged area exhibited marked fibrous proliferation and a disorganized structure, completely lacking the normal cartilage architecture. By the eighth postoperative week, no significant repair of the cartilaginous layer was observed. The defect area remained primarily fibrotic and showed no cartilage-like structures, which was significantly different from that in the sham group. In the scaffold group, repair at the fourth-week post surgery was similar to that in the control group. However, by the eighth week after surgery, some cartilage structures were repaired at the defect site, although the repaired parts were very thin.

In the cell injection group, partial cartilage regeneration was observed at the defect site by the fourth week post operation. The regenerated cartilage was mostly distributed around the periphery of the defect, whereas the center remained predominantly fibrous. By the eighth week post surgery, a thin layer of new cartilage was visible; however, its thickness was still insufficient compared to that of normal cartilage. Additionally, the arrangement of chondrocytes and collagen fibers in the new cartilage was disorganized, and its surface appeared rough.

Significant cartilage reconstruction was observed in the cartilage organoid group by the fourth-week post surgery. Notable new cartilage formation occurred at the center of the defect, although the newly formed chondrocytes and collagen fibers were mostly disorganized and accompanied by fibrous tissue proliferation. The defect area was filled with new cartilage by the eighth week after surgery. The surface was relatively smooth, and the new chondrocytes and collagen fibers aligned perpendicular to the articular surface. Immunohistochemical (IHC) staining was performed to detect Col-II and Aggrecan (Fig. 6(e)). IHC staining and semi-quantitative analysis revealed that consistent with the histological findings, the cartilage organoid group exhibited significantly higher levels of Col-II and ACAN expression at both time points than the control, scaffold, and cell injection groups.

Additionally, the *in vivo* biocompatibility of the implanted cartilage organoids was evaluated. At 4 and 8 weeks postoperatively, H&E staining of major organs from the sham and cartilage organoid implantation groups was performed (Fig. 7(a)). The results showed normal organ structures, indicating that *in vivo* implantation of these organoids is safe and reliable. Furthermore, routine blood analyses and liver and kidney function tests at 4 and 8 weeks postoperatively indicated that the cartilage organoids did not exhibit significant systemic toxicity (Fig. 7(b)).

4 Discussion

The treatment of cartilage defects remains a significant challenge in orthopedic clinical practice and tissue engineering. The avascular nature of cartilage prolongs the repair process and often results in suboptimal outcomes. Additionally, the repair area is predominantly characterized by fibrous tissue proliferation, primarily because the surrounding cartilage progenitor cells exhibit limited chondrogenic potential [40]. Moreover, the repaired tissue in the defect area struggles to integrate structurally with the surrounding normal cartilage [41, 42].

Recent advances in research on cartilage organoids have significantly enhanced the repair of cartilage defects [2, 40, 43–45]. The advantage of this approach lies in utilizing the self-assembly capabilities of stem cells to mimic the natural structure of cartilage in a three-dimensional environment *in vitro* [46]. Current studies on cartilage organoids have been focused on developing innovative scaffold materials that can influence the function of seed cells within the organoids, thereby enhancing the repair of cartilage defects [47]. Engineered seed cells may provide an innovative and alternative approach to research on cartilage organoids.

BMSCs detect external mechanical signals and convert them into cellular responses via specific signal transduction pathways [48]. Studies have demonstrated the feasibility of introducing magnetic nanoparticles into cells and controlling cell behavior through external magnetic fields [6, 49]. These magnetic nanoparticles inherently possess weak magnetic fields that attract each other. This mutual attraction between the engineered MNP-BMSCs, containing magnetic nanoparticles, generates attractive forces. Even without an external magnetic field, these forces feedback into the cells, potentially mediating cell polarization. Transcriptomic analysis was performed to elucidate the potential molecular

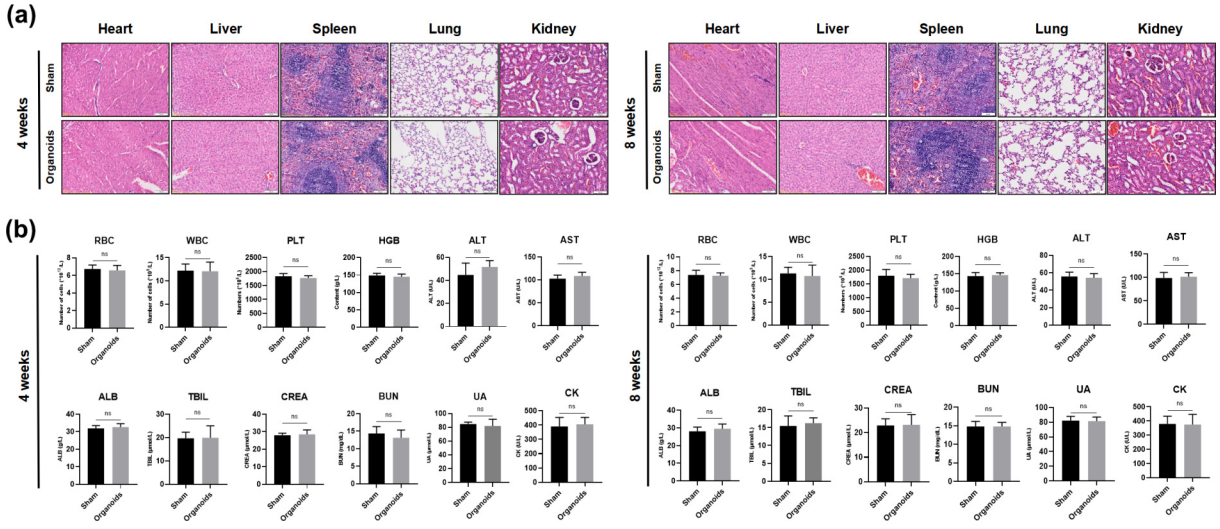

Figure 7 *In vivo* biocompatibility assessment of the improved cartilage organoids. (a) H&E staining of major organs from experimental rats at 4 and 8 weeks post-surgery (scale bars 100 μm). (b) The blood biochemistry, liver and kidney function markers at 4 and 8 weeks post-surgery ($n = 3$).

mechanisms underlying the polarization of engineered MNP-BMSCs. Our results revealed that GO terms related to cell communication, signal transduction, cell adhesion, and cytoskeletal motor activity were closely associated with cell polarity [8, 50–52]. Additionally, the top 3 KEGG pathways included ECM–receptor interaction, regulation of the actin cytoskeleton, and focal adhesion, commonly associated with changes in cell polarity [53–55].

The polarization of BMSCs is closely related to their chondrogenic differentiation, which was further confirmed in our experiments [56–59]. Chondrogenic differentiation of BMSCs involves a multistep process, including cell recruitment, proliferation and migration, cell condensation, chondrogenic differentiation, and chondrocyte maturation [60]. Guided by polarity signals, the engineered MNP-BMSCs demonstrated significantly enhanced migration and invasion capabilities, facilitating cell recruitment and aggregation. We observed that MNP-BMSCs tended to form cell aggregates more readily during chondrogenic differentiation. Even in 2D cultures, these aggregates often formed small cell clusters. These clustered cells expressed higher levels of chondrogenic differentiation-related proteins and produced more cartilage matrix components. Similarly, during 3D chondrogenic differentiation, the collagen content within the chondrospheres was denser, stronger, and less prone to disintegration. These results confirmed that engineered MNP-BMSCs possess enhanced chondrogenic differentiation capabilities and are highly suitable as seed cells for constructing cartilage organoids.

The use of 3D bioprinting technology to construct organoids effectively addresses the issue of disorganized cell distribution in a 3D culture environment and enables the construction of different shapes as needed [61–63]. Alginate and gelatin are hydrogel materials commonly used for organoid construction. They are inexpensive, readily available, and possess excellent biocompatibility [64, 65]. Gelatin, derived from collagen, combines peptides and proteins with repeating amino acid sequences that promote cell adhesion and migration. Its viscosity varies significantly with temperature [66]. In contrast, alginate exhibits excellent printability and mechanical strength, and its viscosity is less affected by temperature [67]. Therefore, combining these two materials in an appropriate ratio results in a mixed hydrogel that exhibits low viscosity at elevated temperatures and shear rates, suitable for extrusion-based 3D bioprinting. Upon cooling, the viscosity increases, which helps maintain the strength of the scaffold during the printing process. Despite the potential dissolution of gelatin during subsequent culture processes, the ionic cross-linking of alginate remains reliable.

Compared to the syringe-based extrusion method, 3D bioprinting technology offers significant advantages. First, the computer-controlled printing system can precisely position the hydrogel, forming a mesh-like structure that improves the overall porosity of the scaffold. This provides a better environment for cell growth within the scaffold, allowing cells to be evenly distributed and avoiding the issue of cell aggregation in specific regions, which can lead to poor growth conditions and cell death. Secondly, 3D bioprinting allows for precise control of the extrusion pressure and speed of bioinks through air pressure. Based on data obtained from preliminary experiments, this significantly reduces the damage caused by shear forces to the cells. In contrast, syringe-based extrusion cannot maintain uniform pressure, and fluctuations in pressure and shear forces can significantly reduce cell viability. Lastly, the organ-like hydrogels constructed by 3D bioprinting are reproducible and have standardized significance. The syringe extrusion method, being reliant on manual operation, offers poor controllability, making it difficult to ensure consistency and precision.

3D bioprinting can generate biomimetic 3D scaffolds with uniform cell distribution, providing spatial depth and enhanced cell-to-cell communication; moreover, it can facilitate the simulation of biological processes in normal tissues [68]. Experiments further confirmed that MNP-BMSCs exhibited a significantly higher chondrogenic differentiation capability in a 3D culture environment compared to a 2D planar culture environment. We employed a layer-by-layer printing strategy to ensure a uniform distribution of MNP-BMSCs within the vertical structure while maintaining adequate porosity. Upon completion of the hydrogel ionic cross-linking, a loose, porous internal structure is maintained, while a thin, low-porosity layer forms on the surface. This configuration restricts the cells within the hydrogel, directing the chondrogenic differentiation of MNP-BMSCs primarily within the vertical stacking structure.

Consequently, the produced collagen and proteoglycans exhibited a vertical distribution, effectively mimicking the middle layer structure of normal cartilage. This longitudinal distribution of the collagen structure was confirmed by the structural analysis of the organoids. Meanwhile, it was observed that organoids not constructed using 3D bioprinting had a loose structure, with collagen fibers showing no clear directional arrangement. Therefore, the application of 3D bioprinting technology for constructing improved cartilage organoids is essential. Further comparison of the three types of seed cells in organoid culture showed that the advanced cartilage organoids constructed with MNPs-BMSCs had significantly enhanced expression of chondrogenic-related proteins and mechanical properties. This evidence underscores the superiority of MNP-BMSCs as seed cells and highlights the critical role of 3D bioprinting in optimizing scaffold architecture to support effective chondrogenic differentiation and tissue integration [61].

Eight weeks after implantation, the advanced cartilage organoids demonstrated impressive cartilage defect repair. Nearly all evaluation metrics indicated an improvement in the healing response. Advanced cartilage organoids significantly improved the repair of cartilage defects by reducing fibrous proliferation and filling the repair area with a more substantial collagen and proteoglycan matrix; this facilitated the subsequent colonization of mature chondrocytes. Additionally, the chondrocytes in the repair area were arranged perpendicular to the joint surface in the newly formed cartilage matrix. We hypothesized that this advantage was due to the vertical cell distribution structure achieved by 3D bioprinting, which shortened the overall tissue repair time [69]. Despite administering more chondrogenic MNP-BMSCs in the simple cell injection group, the repair outcomes were unsatisfactory. This could be because the cells were dispersed throughout the joint cavity, resulting in only a few cells eventually settling in the defect area and contributing to repair. This highlights the advantage of modified cartilage organoids, which can confine most cells to the defect area, significantly enhancing cell utilization and repair efficacy [70]. Although the cartilage repair achieved by advanced cartilage organoids has not yet reached complete restoration, the current results indicate that they have already provided a solid foundation for further development and maturation of new cartilage.

Our study had some limitations. First, although we observed that MNPs influenced cell polarization and conducted transcriptomic sequencing, the detailed underlying molecular mechanisms remain unexplored. In future studies, we will investigate the series of signal transduction and molecular biological processes that occur within cells after MNPs are introduced to elucidate the biological effects of MNPs on BMSCs. Second, we demonstrated effective *in vivo* cartilage repair using a small animal model; however, the experimental duration and sampling points were insufficient to confirm complete cartilage defect repair. Future studies should extend the experimental period and increase the number of sampling time points to further detail and refine the cartilage repair process. Additionally, long-term repair effects in medium-to-large animal models should be explored to simulate the anatomical and functional characteristics of human cartilage more accurately. Third, the cartilage repair process is often complex and involves inflammation, immune responses, apoptosis, and other cellular and biological processes. Future work should build on the current research results to further improve the use of cartilage organoids for cartilage repair, making them more functional and effective. Additionally, although the *in vivo* study results demonstrated excellent repair effects, the comparative effectiveness with other mainstream clinical treatment methods remains uncertain. Future studies should compare our advanced osteochondral organoid method with representative clinical treatments to evaluate its efficacy.

5 Conclusion

In this study, we developed an engineered MNPs-BMSCs-based seed cell and combined it with 3D bioprinting technology to create an advanced cartilage organoid. By introducing MNPs into BMSCs, we constructed engineered MNPs-BMSCs. Under the influence of magnetic forces, these cells undergo polarization. mRNA-seq analysis indicated that the polarization process may be associated with a series of biological processes, including cell adhesion, signal transduction, and cytoskeleton organization. MNP-BMSCs exhibit enhanced migration, aggregation, and chondrogenic differentiation capabilities *in vitro*. Considering these advantages, we used 3D bioprinting technology to employ these cells as seed cells and combined them with optimally proportioned alginate/gelatin hybrid hydrogels to develop advanced cartilage organoids. This organoid mimics the structure of the middle zone of normal cartilage, displaying the expected collagen and proteoglycan distribution and possessing good mechanical properties *in vitro*. Finally, we investigated the *in vivo* cartilage repair capability of the advanced cartilage organoid in a rat femoral cartilage defect model. The results demonstrated significantly enhanced cartilage regeneration and reconstruction of the normal cartilage structure.

This study provides enhanced seed cells for constructing cartilage organoids and introduces new perspectives for stem cell therapy. It presents an innovative strategy for cartilage tissue engineering and demonstrates a wide range of potential applications.

Electronic Supplementary Material: Supplementary material (the IC50 of MNPs on BMSCs; the effect of MNPs on osteogenic differentiation of BMSCs; the effects of MNPs on surface markers of BMSCs; and the design of primer sequences of the genes for RT-qPCR analysis) is available in the online version of this article at https://doi.org/10.26599/NR.2025.94907084.

Data availability

All data needed to support the conclusions in the paper are presented in the manuscript and the Electronic Supplementary Material. Additional data related to this paper may be requested from the corresponding author upon request.

Acknowledgements

This work was financially supported by Science and Technology Innovation Leading Plan of High-Tech Industry in Hunan Province (No. 2020SK2011), The National Natural Science Foundation of China-Youth Science Fund (No. 82204538) and Macao Special Administrative Region Science and Technology Development Fund (No. 0007/2021/AKP).

Declaration of competing interest

All the contributing authors report no conflict of interests in this work.

Author contribution statement

Z. Y. D.: Writing – original draft, writing – review & editing, visualization, validation, project administration, methodology, investigation, formal analysis, data curation, conceptualization. J. J. H.: Writing – review & editing, visualization, methodology, investigation, data curation, conceptualization. Y. J. R.: Writing – original draft, methodology, data cuiation. N. T.: Dats cuiation, methodology. X. L.: Data curation, methodology. H. C. Z.: Methodology. X. C.: Writing – review & editing, supervision, project administration, conceptualization. M. Z.: Writing – review & editing, supervision, resources, conceptualization. S. W.: Review and editing, supervision, resources, conceptualization.

Informed consent

Not applicable.

Ethics statement

The use of 3D bioprinting technology to construct organoids effectively addresses the issue of disorganized cell distribution in a 3D culture environment and enables the construction of different shapes as needed [61–63]. Alginate and gelatin are hydrogel materials commonly used for organoid construction. They are inexpensive, readily available, and possess excellent biocompatibility [64, 65]. Gelatin, derived from collagen, combines peptides and proteins with repeating amino acid sequences that promote cell adhesion and migration. Its viscosity varies significantly with temperature [66]. In contrast, alginate exhibits excellent printability and mechanical strength, and its viscosity is less affected by temperature [67]. Therefore, combining these two materials in an appropriate ratio results in a mixed hydrogel that exhibits low viscosity at elevated temperatures and shear rates, suitable for extrusion-based 3D bioprinting. Upon cooling, the viscosity increases, which helps maintain the strength of the scaffold during the printing process. Despite the potential dissolution of gelatin during subsequent culture processes, the ionic cross-linking of alginate remains reliable.

The studies have been approved by a research ethics committee at the Experimental Animal Center of Central South University (XMSB-2023-0022).

Use of AI statement

None.

References

[1] Li, S. A.; Niu, D. W.; Fang, H. W.; Chen, Y. C.; Li, J. Y.; Zhang, K. X.; Yin, J. B.; Fu, P. L. Tissue adhesive, ROS scavenging and injectable PRP-based 'plasticine' for promoting cartilage repair. *Regen. Biomater.* **2024**, *11*, rbad104.

[2] Shen, C. Y.; Wang, J.; Li, G. F.; Hao, S. Y.; Wu, Y.; Song, P. R.; Han, Y. F.; Li, M. M.; Wang, G. C.; Xu, K. et al. Boosting cartilage repair with silk fibroin-DNA hydrogel-based cartilage organoid precursor. *Bioact. Mater.* **2024**, *35*, 429–444.

[3] Nordberg, R. C.; Bielajew, B. J.; Takahashi, T.; Dai, S. Y.; Hu, J. C.; Athanasiou, K. A. Recent advancements in cartilage tissue engineering innovation and translation. *Nat. Rev. Rheumatol.* **2024**, *20*, 323–346.

[4] Lee, E.; Epanomeritakis, I. E.; Lu, V.; Khan, W. Bone marrow-derived mesenchymal stem cell implants for the treatment of focal chondral defects of the knee in animal models: A systematic review and meta-analysis. *Int. J. Mol. Sci.* **2023**, *24*, 3227.

[5] Mamidi, M. K.; Das, A. K.; Zakaria, Z.; Bhonde, R. Mesenchymal stromal cells for cartilage repair in osteoarthritis. *Osteoarthr. Cartil.* **2016**, *24*, 1307–1316.

[6] Deng, C. J.; Li, Z. G.; Lu, L. Y.; Zhang, H. N.; Chen, R. Z.; Liu, Y. L.; Tong, Y. F.; Fan, O. R.; Huang, W. X.; Sun, Y. E. et al. Sophisticated magneto-mechanical actuation promotes *in situ* stem cell assembly and chondrogenesis for treating osteoarthritis. *ACS Nano* **2023**, *17*, 21690–21707.

[7] Wang, S. Q.; Yang, L. T.; Cai, B. L.; Liu, F. W.; Hou, Y. N.; Zheng, H.; Cheng, F.; Zhang, H. P.; Wang, L.; Wang, X. Y. et al. Injectable hybrid inorganic nanoscaffold as rapid stem cell assembly template for cartilage repair. *Natl. Sci. Rev.* **2022**, *9*, nwac037.

[8] Butler, M. T.; Wallingford, J. B. Planar cell polarity in development and disease. *Nat. Rev. Mol. Cell Biol.* **2017**, *18*, 375–388.

[9] Yamashita, Y. M.; Yuan, H. B.; Cheng, J.; Hunt, A. J. Polarity in stem cell division: Asymmetric stem cell division in tissue homeostasis. *Cold Spring Harb. Perspect. Biol.* **2010**, *2*, a001313.

[10] Kim, E. J. Y.; Korotkevich, E.; Hiiragi, T. Coordination of cell polarity, mechanics and fate in tissue self-organization. *Trends Cell Biol.* **2018**, *28*, 541–550.

[11] Alagiri, M.; Muthamizhchelvan, C.; Ponnusamy, S. Structural and magnetic properties of iron, cobalt and nickel nanoparticles. *Synth. Met.* **2011**, *161*, 1776–1780.

[12] Farzin, A.; Etesami, S. A.; Quint, J.; Memic, A.; Tamayol, A. Magnetic nanoparticles in cancer therapy and diagnosis. *Adv. Healthc. Mater.* **2020**, *9*, 1901058.

[13] Chen, Y. L.; Hou, S. K. Application of magnetic nanoparticles in cell therapy. *Stem. Cell Res. Ther.* **2022**, *13*, 135.

[14] Bianchi, E.; Vigani, B.; Viseras, C.; Ferrari, F.; Rossi, S.; Sandri, G. Inorganic nanomaterials in tissue engineering. *Pharmaceutics* **2022**, *14*, 1127.

[15] Zhou, C. C.; Wang, C. L.; Xu, K.; Niu, Z. X.; Zou, S. J.; Zhang, D. M.; Qian, Z. Y.; Liao, J. F.; Xie, J. Hydrogel platform with tunable stiffness based on magnetic nanoparticles cross-linked GelMA for cartilage regeneration and its intrinsic biomechanism. *Bioact. Mater.* **2023**, *25*, 615–628.

[16] Lin, T.; Zhao, Y.; Chen, J. L.; Wu, C. X.; Li, Z.; Cao, Y. M.; Lu, R.; Zhang, J. W.; Zhao, C.; Lu, Y. Carboxymethyl chitosan-assisted MnO_x nanoparticles: Synthesis, characterization, detection and cartilage repair in early osteoarthritis. *Carbohydr. Polym.* **2022**, *294*, 119821.

[17] Go, G.; Han, J. W. N.; Zhen, J.; Zheng, S. H.; Yoo, A.; Jeon, M. J.; Park, J. O.; Park, S. A magnetically actuated microscaffold containing mesenchymal stem cells for articular cartilage repair. *Adv. Healthc. Mater.* **2017**, *6*, 1601378.

[18] Zhang, N. Y.; Lock, J.; Sallee, A.; Liu, H. N. Magnetic nanocomposite hydrogel for potential cartilage tissue engineering: Synthesis, characterization, and cytocompatibility with bone marrow derived mesenchymal stem cells. *ACS Appl. Mater. Interfaces* **2015**, *7*, 20987–20998.

[19] Kunze, A.; Tseng, P.; Godzich, C.; Murray, C.; Caputo, A.; Schweizer, F. E.; Di Carlo, D. Engineering cortical neuron polarity with nanomagnets on a chip. *ACS Nano* **2015**, *9*, 3664–3676.

[20] Kim, Y. J.; Lee, D. B.; Jeong, E.; Jeon, J. Y.; Kim, H. D.; Kang, H. E. M.; Kim, Y. K. Magnetically stimulated integrin binding alters cell polarity and affects epithelial-mesenchymal plasticity in metastatic cancer cells. *ACS Appl. Mater. Interfaces* **2024**, *16*, 8365–8377.

[21] Clevers, H. Modeling development and disease with organoids. *Cell* **2016**, *165*, 1586–1597.

[22] Takebe, T.; Wells, J. M. Organoids by design. *Science* **2019**, *364*, 956–959.

[23] Hu, Y.; Zhang, H.; Wang, S. C.; Cao, L. H.; Zhou, F. J.; Jing, Y. Y.; Su, J. C. Bone/cartilage organoid on-chip: Construction strategy and application. *Bioact. Mater.* **2023**, *25*, 29–41.

[24] Dönges, L.; Damle, A.; Mainardi, A.; Bock, T.; Schönenberger, M.; Martin, I.; Barbero, A. Engineered human osteoarthritic cartilage organoids. *Biomaterials* **2024**, *308*, 122549.

[25] X.; Hu, D. A.; Wu, D.; He, F.; Wang, H.; Huang, L. J.; Shi, D. Y.; Liu, Q.; Ni, N.; Pakvasa, M. et al. Applications of biocompatible scaffold materials in stem cell-based cartilage tissue engineering. *Front. Bioeng. Biotechnol.* **2021**, *9*, 603444.

[26] Ding, Z. Y.; Tang, N.; Huang, J. J.; Cao, X.; Wu, S. Global hotspots and emerging trends in 3D bioprinting research. *Front. Bioeng. Biotechnol.* **2023**, *11*, 1169893.

[27] Zhang, Y.; Li, G. F.; Wang, J.; Zhou, F. J.; Ren, X. X.; Su, J. C. Small joint organoids 3D bioprinting: Construction strategy and application. *Small* **2024**, *20*, 2302506.

[28] Łabowska, M. B.; Cierluk, K.; Jankowska, A. M.; Kulbacka, J.; Detyna, J.; Michalak, I. A review on the adaption of alginate-gelatin hydrogels for 3D cultures and bioprinting. *Materials (Basel)* **2021**, *14*, 858.

[29] Xia, H. S.; Liang, C.; Luo, P.; Huang, J. J.; He, J. S.; Wang, Z. L.; Cao, X.; Peng, C.; Wu, S. Pericellular collagen I coating for enhanced homing and chondrogenic differentiation of mesenchymal stem cells in direct intra-articular injection. *Stem. Cell Res. Ther.* **2018**, *9*, 174.

[30] Cui, Z.; Zhou, L. P.; Huang, J. J.; Xu, L.; Ding, Z. Y.; Hu, H.; Cao, X.; Zhao, M.; Wu, S. Dual-model biomanufacturing of porous biomimetic scaffolds with concentrated growth factors and embedded endothelial vascular channels for bone defect regeneration. *Chem. Eng. J.* **2024**, *483*, 148933.

[31] Rarokar, N.; Yadav, S.; Saoji, S.; Bramhe, P.; Agade, R.; Gurav, S.; Khedekar, P.; Subramaniyan, V.; Wong, L. S.; Kumarasamy, V. Magnetic nanosystem a tool for targeted delivery and diagnostic application: Current challenges and recent advancement. *Int. J. Pharm. X* **2024**, *7*, 100231.

[32] Zhang, S. L.; Li, J.; Lykotrafitis, G.; Bao, G.; Suresh, S. Size-dependent endocytosis of nanoparticles. *Adv. Mater.* **2009**, *21*, 419–424.

[33] Yu, C. C.; Yang, W. T.; Yang, L. J.; Ye, L.; Sun, R. T.; Gu, T. Y.; Ying, X. Z.; Wang, M. N.; Tang, R. K.; Fan, S. W. et al. Synergistic effect of magneto-mechanical bioengineered stem cells and magnetic field to alleviate osteoporosis. *ACS Appl. Mater. Interfaces* **2023**, *15*, 19976–19988.

[34] Miao, Y. C.; Pourquié, O. Cellular and molecular control of vertebrate somitogenesis. *Nat. Rev. Mol. Cell Biol.* **2024**, *25*, 517–533.

[35] Andrews, M. G.; Subramanian, L.; Salma, J.; Kriegstein, A. R. How mechanisms of stem cell polarity shape the human cerebral cortex. *Nat. Rev. Neurosci.* **2022**, *23*, 711–724.

[36] Wodarz, A.; Näthke, I. Cell polarity in development and cancer. *Nat. Cell Biol.* **2007**, *9*, 1016–1024.
[37] Akilbekova, D.; Shaimerdenova, M.; Adilov, S.; Berillo, D. Biocompatible scaffolds based on natural polymers for regenerative medicine. *Int. J. Biol. Macromol.* **2018**, *114*, 324–333.
[38] Guillén-Carvajal, K.; Valdez-Salas, B.; Beltrán-Partida, E.; Salomón-Carlos, J.; Cheng, N. Chitosan, gelatin, and collagen hydrogels for bone regeneration. *Polymers (Basel)* **2023**, *15*, 2762.
[39] Zhao, L. L.; Zhou, Y. F.; Zhang, J. Y.; Liang, H. Z.; Chen, X. W.; Tan, H. Natural polymer-based hydrogels: From polymer to biomedical applications. *Pharmaceutics* **2023**, *15*, 2514.
[40] Abe, K.; Yamashita, A.; Morioka, M.; Horike, N.; Takei, Y.; Koyamatsu, S.; Okita, K.; Matsuda, S.; Tsumaki, N. Engraftment of allogeneic iPS cell-derived cartilage organoid in a primate model of articular cartilage defect. *Nat. Commun.* **2023**, *14*, 804.
[41] Huey, D. J.; Hu, J. C.; Athanasiou, K. A. Unlike bone, cartilage regeneration remains elusive. *Science* **2012**, *338*, 917–921.
[42] Tognana, E.; Chen, F.; Padera, R. F.; Leddy, H. A.; Christensen, S. E.; Guilak, F.; Vunjak-Novakovic, G.; Freed, L. E. Adjacent tissues (cartilage, bone) affect the functional integration of engineered calf cartilage *in vitro*. *Osteoarthritis Cartilage* **2005**, *13*, 129–138.
[43] Yang, Z.; Wang, B.; Liu, W.; Li, X. K.; Liang, K. N.; Fan, Z. J.; Li, J. J.; Niu, Y. D.; He, Z. H.; Li, H. et al. *In situ* self-assembled organoid for osteochondral tissue regeneration with dual functional units. *Bioact. Mater.* **2023**, *27*, 200–215.
[44] Zhou, Z. Y.; Song, P. R.; Wu, Y.; Wang, M. M.; Shen, C. Y.; Ma, Z. X.; Ren, X. X.; Wang, X. H.; Chen, X.; Hu, Y. et al. Dual-network DNA-silk fibroin hydrogels with controllable surface rigidity for regulating chondrogenic differentiation. *Mater. Horiz.* **2024**, *11*, 1465–1483.
[45] Hall, G. N.; Tam, W. L.; Andrikopoulos, K. S.; Casas-Fraile, L.; Voyiatzis, G. A.; Geris, L.; Luyten, F. P.; Papantoniou, I. Patterned, organoid-based cartilaginous implants exhibit zone specific functionality forming osteochondral-like tissues *in vivo*. *Biomaterials* **2021**, *273*, 120820.
[46] Zhao, Z. X.; Chen, X. Y.; Dowbaj, A. M.; Sljukic, A.; Bratlie, K.; Lin, L. D.; Fong, E. L. S.; Balachander, G. M.; Chen, Z. W.; Soragni, A. et al. Organoids. *Nat. Rev. Methods Primers* **2022**, *2*, 94.
[47] Li, X. L.; Sheng, S. H.; Li, G. F.; Hu, Y.; Zhou, F. J.; Geng, Z.; Su, J. C. Research progress in hydrogels for cartilage organoids. *Adv. Healthc. Mater.* **2024**, *13*, 2400431.
[48] Hao, J.; Zhang, Y. L.; Jing, D.; Shen, Y.; Tang, G.; Huang, S. S.; Zhao, Z. H. Mechanobiology of mesenchymal stem cells: Perspective into mechanical induction of MSC fate. *Acta Biomater.* **2015**, *20*, 1–9.
[49] Goršak, T.; Jovičić, E. J.; Tratnjek, L.; Križaj, I.; Sepulveda, B.; Nogues, J.; Kreft, M. E.; Petan, T.; Kralj, S.; Makovec, D. The efficient magneto-mechanical actuation of cancer cells using a very low concentration of non-interacting ferrimagnetic hexaferrite nanoplatelets. *J. Colloid Interface Sci.* **2024**, *657*, 778–787.
[50] Bloch, D.; Yalovsky, S. Cell polarity signaling. *Curr. Opin. Plant Biol.* **2013**, *16*, 734–742.
[51] Ebnet, K.; Kummer, D.; Steinbacher, T.; Singh, A.; Nakayama, M.; Matis, M. Regulation of cell polarity by cell adhesion receptors. *Semin. Cell Dev. Biol.* **2018**, *81*, 2–12.
[52] Blanchoin, L.; Boujemaa-Paterski, R.; Sykes, C.; Plastino, J. Actin dynamics, architecture, and mechanics in cell motility. *Physiol. Rev.* **2014**, *94*, 235–263.
[53] Holmes, W. R.; Park, J.; Levchenko, A.; Edelstein-Keshet, L. A mathematical model coupling polarity signaling to cell adhesion explains diverse cell migration patterns. *PLoS Comput. Biol.* **2017**, *13*, e1005524.
[54] Raman, R.; Pinto, C. S.; Sonawane, M. Polarized organization of the cytoskeleton: Regulation by cell polarity proteins. *J. Mol. Biol.* **2018**, *430*, 3565–3584.
[55] Fischer, R. S.; Sun, X. Y.; Baird, M. A.; Hourwitz, M. J.; Seo, B. R.; Pasapera, A. M.; Mehta, S. B.; Losert, W.; Fischbach, C.; Fourkas, J. T. et al. Contractility, focal adhesion orientation, and stress fiber orientation drive cancer cell polarity and migration along wavy ECM substrates. *Proc. Natl. Acad. Sci. USA* **2021**, *118*, e2021135118.
[56] Woods, A.; Wang, G. Y.; Beier, F. Regulation of chondrocyte differentiation by the actin cytoskeleton and adhesive interactions. *J. Cell. Physiol.* **2007**, *213*, 1–8.
[57] Huang, D. Y.; Li, Y. H.; Ma, Z. H.; Lin, H.; Zhu, X. D.; Xiao, Y.; Zhang, X. D. Collagen hydrogel viscoelasticity regulates MSC chondrogenesis in a ROCK-dependent manner. *Sci. Adv.* **2023**, *9*, eade9497.
[58] Guo, J. Q.; Wang, F. B.; Huang, Y. M.; He, H. J.; Tan, W. Y.; Yi, M. H.; Egelman, E. H.; Xu, B. Cell spheroid creation by transcytotic intercellular gelation. *Nat. Nanotechnol.* **2023**, *18*, 1094–1104.
[59] Bradley, E. W.; Drissi, M. H. Wnt5b regulates mesenchymal cell aggregation and chondrocyte differentiation through the planar cell polarity pathway. *J. Cell. Physiol.* **2011**, *226*, 1683–1693.
[60] Hodgkinson, T.; Kelly, D. C.; Curtin, C. M.; O'Brien, F. J. Mechanosignalling in cartilage: An emerging target for the treatment of osteoarthritis. *Nat. Rev. Rheumatol.* **2022**, *18*, 67–84.
[61] Tang, X. Y.; Wu, S. S.; Wang, D.; Chu, C.; Hong, Y.; Tao, M. D.; Hu, H.; Xu, M.; Guo, X.; Liu, Y. Human organoids in basic research and clinical applications. *Signal Transduct. Target. Ther.* **2022**, *7*, 168.
[62] Correia Carreira, S.; Begum, R.; Perriman, A. W. 3D bioprinting: The emergence of programmable biodesign. *Adv. Healthc. Mater.* **2020**, *9*, 1900554.
[63] Ren, Y.; Yang, X.; Ma, Z. J.; Sun, X.; Zhang, Y. X.; Li, W. T.; Yang, H.; Qiang, L.; Yang, Z. Z.; Liu, Y. H. et al. Developments and opportunities for 3D bioprinted organoids. *Int. J. Bioprint.* **2021**, *7*, 364.
[64] Nerger, B. A.; Sinha, S.; Lee, N. N.; Cheriyan, M.; Bertsch, P.; Johnson, C. P.; Mahadevan, L.; Bonventre, J. V.; Mooney, D. J. 3D hydrogel encapsulation regulates nephrogenesis in kidney organoids. *Adv. Mater.* **2024**, *36*, 2308325.
[65] Carpentier, N.; Ye, S. C.; Delemarre, M. D.; Van der Meeren, L.; Skirtach, A. G.; van der Laan, L. J. W.; Schneeberger, K.; Spee, B.; Dubruel, P.; Van Vlierberghe, S. Gelatin-based hybrid hydrogels as matrices for organoid culture. *Biomacromolecules* **2024**, *25*, 590–604.
[66] Liu, D. S.; Nikoo, M.; Boran, G.; Zhou, P.; Regenstein, J. M. Collagen and gelatin. *Annu. Rev. Food Sci. Technol.* **2015**, *6*, 527–557.
[67] Rastogi, P.; Kandasubramanian, B. Review of alginate-based hydrogel bioprinting for application in tissue engineering. *Biofabrication* **2019**, *11*, 042001.
[68] Matai, I.; Kaur, G.; Seyedsalehi, A.; McClinton, A.; Laurencin, C. T. Progress in 3D bioprinting technology for tissue/organ regenerative engineering. *Biomaterials* **2020**, *226*, 119536.
[69] Bhumiratana, S.; Eton, R. E.; Oungoulian, S. R.; Wan, L. Q.; Ateshian, G. A.; Vunjak-Novakovic, G. Large, stratified, and mechanically functional human cartilage grown in vitro by mesenchymal condensation. *Proc. Natl. Acad. Sci. USA* **2014**, *111*, 6940–6945.
[70] Anderson, J. A.; Little, D.; Toth, A. P.; Moorman, C. T.; Tucker, B. S.; Ciccotti, M. G.; Guilak, F. Stem cell therapies for knee cartilage repair: The current status of preclinical and clinical studies. *Am. J. Sports Med.* **2014**, *42*, 2253–2261.